Prediction of the 14 June 2010 Oklahoma City Extreme Precipitation and Flooding Event in a Multiphysics Multi-Initial-Conditions Storm-Scale Ensemble Forecasting System

NATHAN DAHL AND MING XUE

Center for Analysis and Prediction of Storms, and School of Meteorology, University of Oklahoma, Norman, Oklahoma

(Manuscript received 5 September 2015, in final form 18 April 2016)

ABSTRACT

Prolonged heavy rainfall produced widespread flooding in the Oklahoma City area early on 14 June 2010. This event was poorly predicted by operational models; however, it was skillfully predicted by the Storm-Scale Ensemble Forecast produced by the Center for Analysis and Prediction of Storms as part of the Hazardous Weather Testbed 2010 Spring Experiment. In this study, the quantitative precipitation forecast skill of ensemble members is assessed and ranked using a neighborhood-based threat score calculated against the stage IV precipitation data, and Oklahoma Mesonet observations are used to evaluate the forecast skill for surface conditions. Statistical correlations between skill metrics and qualitative comparisons of relevant features for higher- and lower-ranked members are used to identify important processes. The results demonstrate that the development of a cold pool from previous convection and the movement and orientation of the associated outflow boundary played dominant roles in the event. Without assimilated radar data from this earlier convection, the modeled cold pool was too weak and too slow to develop. Furthermore, forecast skill was sensitive to the choice of microphysics parameterization; members that used the Thompson scheme produced initial cold pools that propagated too slowly, substantially increasing errors in the timing and placement of later precipitation. The results also suggest important roles played by finescale, transient features in the period of outflow boundary stalling and reorientation associated with the heaviest rainfall. The unlikelihood of a deterministic forecast reliably predicting these features highlights the benefit of using convection-allowing/convection-resolving ensemble forecast methods for events of this kind.

1. Introduction

As noted in Doswell et al. (1996), C. F. Chappell condensed the key issues affecting extreme rainfall events into the simple axiom that "the heaviest precipitation occurs where the rainfall rate is the highest for the longest period of time." A variety of mechanisms exist at different spatial and temporal scales for producing persistent rainfall over a given area, including synoptically driven convection [accounting for 27% of surveyed extreme rain events in Schumacher and Johnson (2005) and 37% in Heideman and Fritsch (1988)], orographic lift (11% in Heideman and Fritsch), and tropical cyclones approaching land (8% in Schumacher and Johnson; 1% in Heideman and Fritsch). While these proportions vary somewhat from survey to survey, there is a general consensus that the majority of extreme rain events in the United States are associated with mesoscale convective systems (MCSs), with Schumacher and Johnson reporting 66% and Heideman and Fritsch reporting 51%. (It should be noted that the latter statistic includes events arising from seabreeze fronts, drylines, and remnant boundaries, which account for 16%, 1%, and 4% of the events in the Heideman and Fritsch survey, respectively. This is done to maintain consistency with the Schumacher and Johnson survey, which classifies any event extending >100 km in at least one direction and with a duration of between 3 and 24 h as an MCS.)

The development and maintenance of MCSs is significantly affected by phenomena that pose particular challenges for numerical weather prediction models. For example, Clark et al. (2010b) note from previous studies that convection-parameterizing models do not reliably capture the evolution of features such as

Corresponding author address: Nathan Dahl, RSMAS/MPO, 4600 Rickenbacker Cswy., Miami, FL 33149.
E-mail: ndahl@rsmas.miami.edu

DOI: 10.1175/WAF-D-15-0116.1

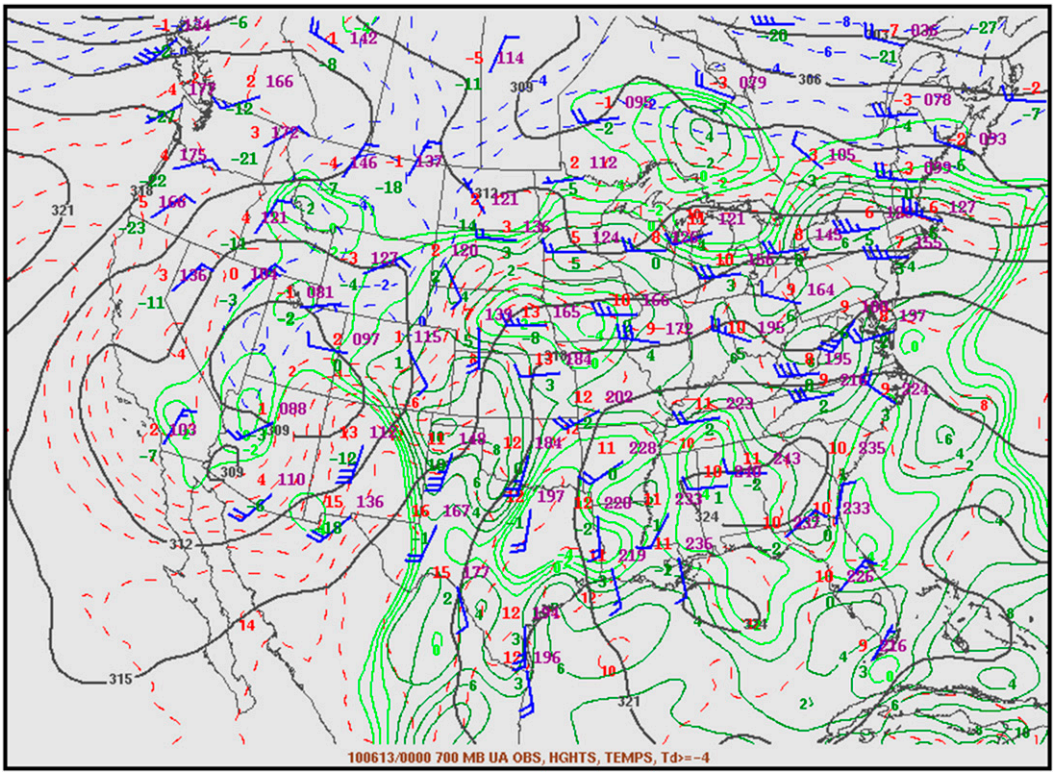

FIG. 1. Analyzed 700-hPa temperature (red dashed contours), height (solid black contours), and observed winds from NWS soundings valid 0000 UTC 13 Jun 2010. [Image taken from the Storm Prediction Center severe weather event archive (http://www.spc.noaa.gov/exper/archive/events/).]

cold pools and outflow boundaries (Davis et al. 2003; Molinari and Dudek 1992; Bukovsky et al. 2006). On the other hand, the skill of deterministic models operating at convection-allowing scales is hindered by the rapid growth of errors stemming from insufficient data sampling and the chaotic unresolved behavior of small-scale convection (Kong et al. 2006, 2007; Zhang et al. 2006; Hohenegger and Schär 2007).

These difficulties have motivated a recent emphasis on probabilistic techniques employing forecast ensembles. When model and observation uncertainties are adequately represented by the ensemble distribution, ensemble methods have been shown to improve the reliability of forecasts of mesoscale convective phenomena, particularly when the ensemble is run at a convection-allowing resolution or higher (Clark et al. 2009). One example is the Storm Scale Ensemble Forecast (SSEF) produced in recent years by the Center for Analysis and Prediction of Storms (CAPS). During the 2010 Hazardous Weather Testbed (HWT) Spring Experiment, CAPS SSEF mean and probability-matched mean quantitative precipitation forecasts (QPFs) outperformed operational deterministic and ensemble forecasts for several MCS-driven heavy rain events in the central and southern plains, including the 14 June 2010 Oklahoma City, Oklahoma, metropolitan area flood (Xue et al. 2010).

Along with improvements in forecast quality, ensemble approaches also provide opportunities for postevent analysis of MCS behaviors. A single model run may not reliably predict the features responsible for the evolution of an MCS, and the role played by such features in the general progression of the event may not be firmly established even if the model successfully produces them. However, in an ensemble of sufficient size, correlations may be drawn that can serve to highlight the importance of relevant features and suggest which variations do not substantially affect the forecast skill. For example, Clark et al. (2010b) used probabilistic analysis of convection-parameterizing and convection-allowing ensemble forecasts to analyze the vorticity budget of a mesoscale convective vortex associated with a regional severe weather event on 1 June 2007. More recently, Schumacher et al. (2013) used a neighborhood-based threat score (see Clark et al. 2010a) to rank the overall QPF skill of the CAPS SSEF members for a heavy rainfall event associated with a slow-moving mesoscale convective vortex over eastern Texas and western Arkansas on 9–11 June 2010. The results enabled them to efficiently isolate patterns

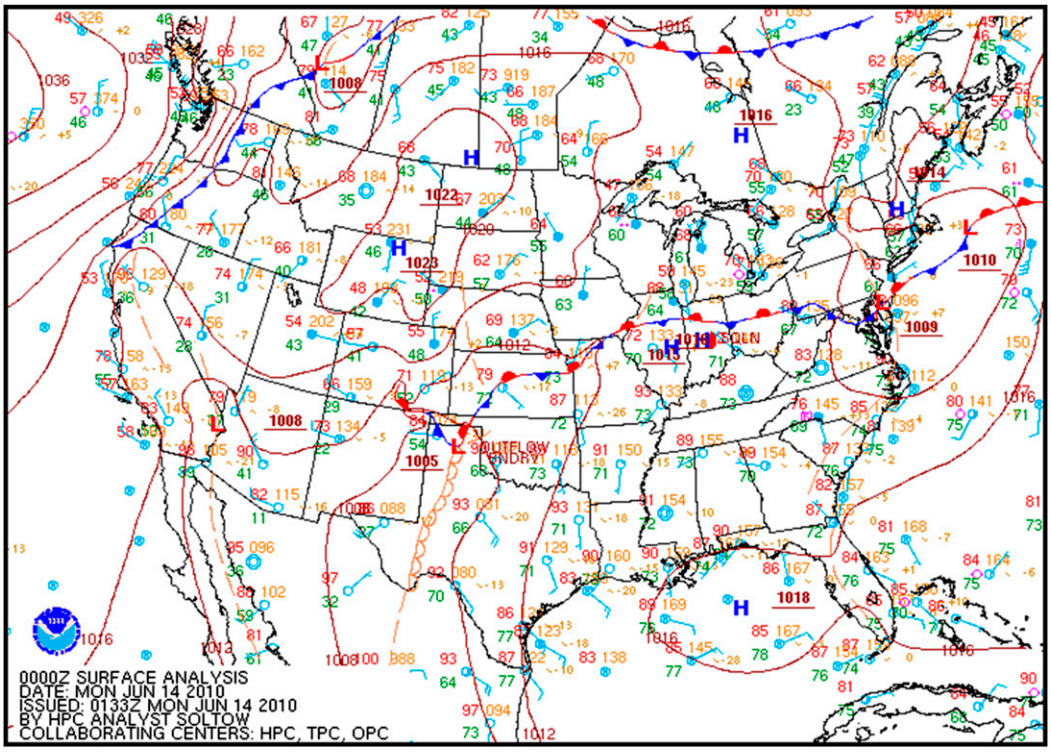

FIG. 2. Hydrometerological Prediction Center (HPC) surface analysis valid 0000 UTC 14 Jun 2010. (Image taken from the Storm Prediction Center severe weather event archive.)

relating member settings (e.g., PBL or microphysics parameterizations) and the treatment of features of interest (e.g., the low-level jet) to model skill, facilitating the development of a conceptual model for the event. Other examples of ensemble-based analysis of mesoscale convective events include Hawblitzel et al. (2007), Martin and Xue (2006), Schumacher (2011), Bednarczyk and Ancell (2015), and Torn and Romine (2015).

The success of the above approach and the demonstrated skill of the CAPS SSEF motivate the examination presented here of the 14 June 2010 extreme rain event. The analysis begins with a synoptic and mesoscale overview in section 2. Section 3 provides a summary of CAPS SSEF real-time products and a description of the methods employed in the analysis. Section 4 describes and discusses the results of the analysis. Finally, conclusions and suggestions for possible future work are provided in section 5.

2. The 14 June 2010 Oklahoma City extreme rain and flooding event

a. *Synopsis*

Under the influence of entrenched high pressure to the east and a slow-moving cutoff low to the west (as seen on the 700-hPa chart in Fig. 1), the southern plains received sustained deep moisture advection from the Gulf of Mexico from late 11 June through late 13 June. A broad region of moderate instability with high precipitable water content resulted, with sounding-derived values for convective available potential energy in the most unstable parcels (MUCAPE) exceeding 2000 J kg^{-1} across the region at 0000 UTC 14 June. Meanwhile, outflow from a series of MCSs in the central plains produced a stationary boundary extending from the Great Lakes region into the Texas and Oklahoma Panhandles (Fig. 2).

The intersection of the outflow boundary in the northern Texas Panhandle and a dryline extending southward into west-central Texas provided a focus for organized convection on the afternoon and evening of 13 June. A cluster of cells quickly coalesced into a trailing-stratiform MCS (archetype described in Parker and Johnson 2000) and moved east-southeastward into north-central Oklahoma under the influence of an extensive cold pool. At this point, conditions resembled the ''mesohigh'' flash flood model diagrammed by Maddox et al. (1979) with substantial midlevel directional shear shifting the winds from across boundary at low levels to along boundary at upper levels. Meanwhile, with large-scale ascent limited, convection south

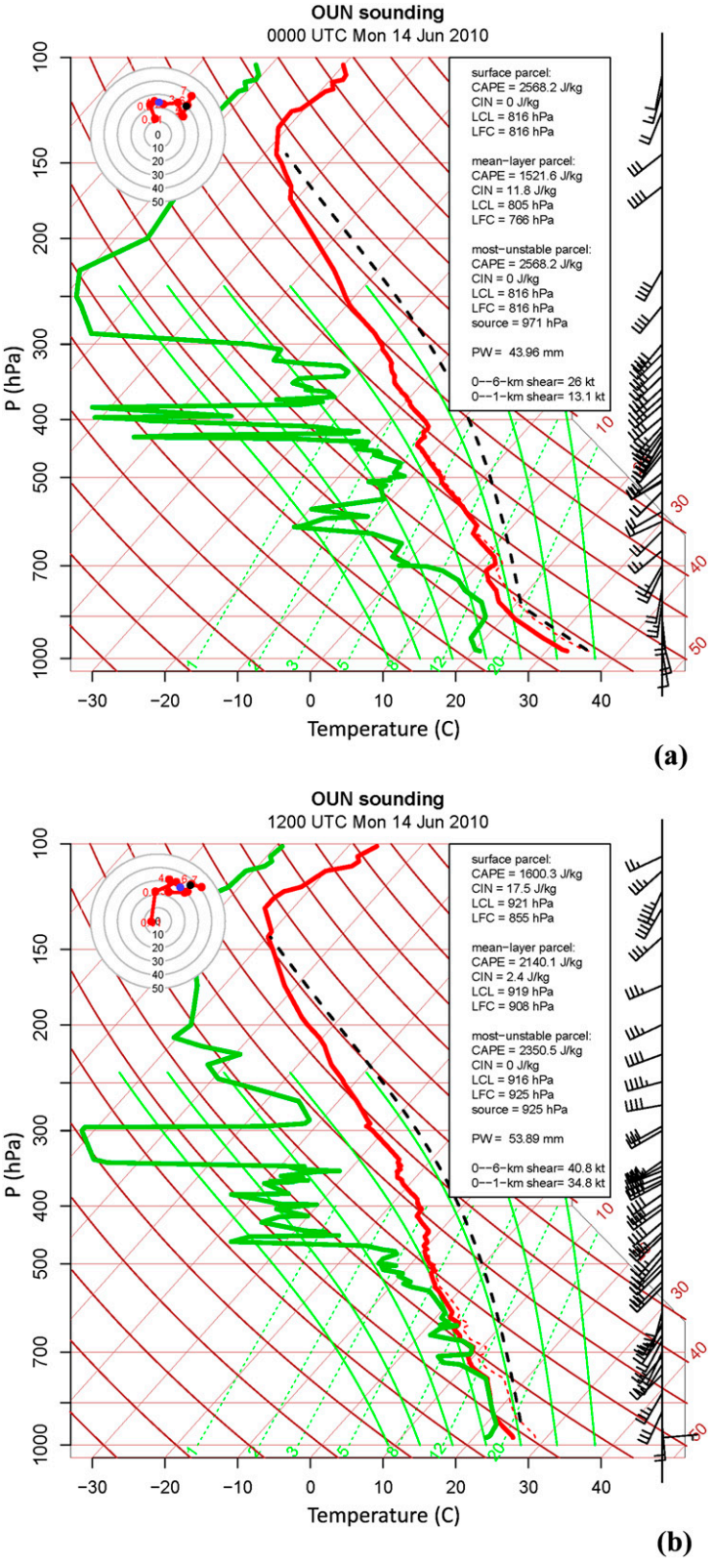

FIG. 3. The (a) 0000 and (b) 1200 UTC 14 Jun 2010 soundings taken at OUN (red dot in Fig. 4). Red dotted lines are environmental virtual temperature profiles, black dashed lines are most unstable parcel virtual temperature trajectories, and blue and black dots on the hodographs indicate winds at roughly 850 and 500 mb, respectively. (Plots courtesy of R. Schumacher.)

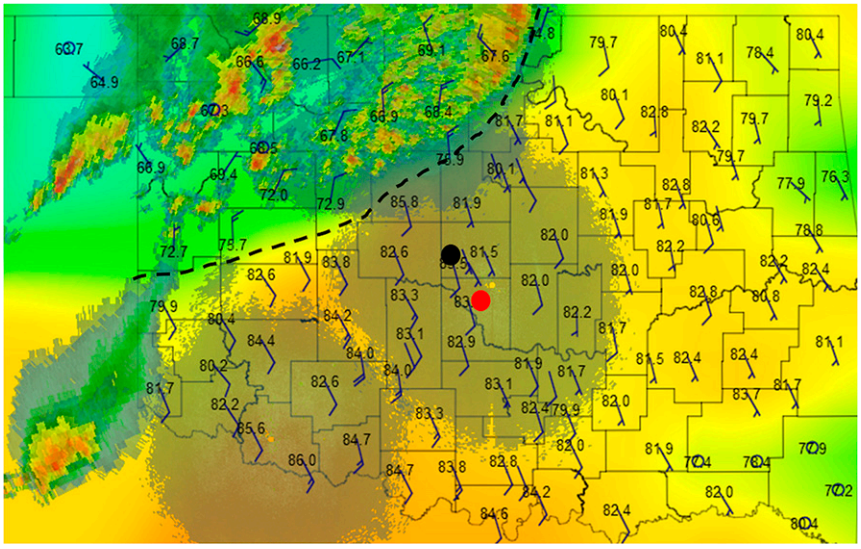

FIG. 4. Radar reflectivity mosaic from Vance (KVNX), Twin Lakes (KTLX), and Frederick (KFDR) WSR-88Ds overlaid on 1.5 m AGL temperature (numbers and color-filled contours in °F) and wind (barbs in kt, where 1 kt = 0.51 m s^{-1}) observations from the Oklahoma Mesonet for 0330 UTC 14 Jun 2010. The dashed line marks the approximate location of the outflow boundary, the black dot marks the location of Oklahoma City, and the red dot marks the location of Norman.

of the outflow boundary–dryline triple point was sporadic, leaving the moist, unstable air mass in central and southwest Oklahoma largely undisturbed on 13 June, with only weak mean-layer convective inhibition in place and no convective inhibition in the most unstable parcels (MUCINH) as shown in the 0000 UTC 14 June sounding for Norman, Oklahoma (OUN), in Fig. 3a.

Overnight, moisture advection and evaporative cooling from dissipating clouds moving in from the southwest eroded the remaining inhibition and increased the precipitable water content to over 50 mm [well above the 99th percentile from local and seasonal climatology as noted in Basara et al. (2011)], as shown in the 1200 UTC 14 June OUN sounding in Fig. 3b. Moreover, nocturnal strengthening and veering (see Blackadar 1957) kept the low-level jet oriented at a large angle to the outflow boundary (with south-southwesterly 850-hPa winds approaching 20 m s^{-1}) and reduced the speed and directional shear in the midlevels (cf. the hodographs in Fig. 3). These ingredients indicate a highly favorable environment for a heavy rain event, with enhanced low-level advection of very moist, unstable air into a region of forced ascent over a slow-moving boundary (e.g., Junker et al. 1999; Moore et al. 2003; Schumacher and Johnson 2005). However, explaining the magnitude and specific location of the observed rainfall maximum requires additional examination.

b. *Analysis of outflow boundary progression and impacts on later convection*

The manner in which the outflow boundary associated with the convection from late 13 June progressed through central Oklahoma appears to have been critical to the development of the extreme precipitation in the Oklahoma City area early on 14 June. Analysis of cold pool motion is often hindered by lack of resolution in surface station observations; fortunately, this particular event occurred in a region well sampled by both the Oklahoma Mesonet and the WSR-88D network (specifically the radars at Vance, Twin Lakes, and Frederick in Oklahoma). Therefore, the evaluation of the motion of the cold pool in the numerical models is well facilitated in this case.

The progress of the outflow boundary through Oklahoma is visually tracked in this study using 10-m wind barbs along with 2-m potential temperature contours derived from the Oklahoma Mesonet observations. Figure 4 shows that the outflow boundary (black dashed line) initially curved from an east–west orientation on the southern flank to a more north–south orientation near the leading edge on the eastern flank. In the hours preceding the onset of sustained heavy rain in Oklahoma City at 0930 UTC, the eastern portion of the cold pool advanced rapidly southeastward (red arrows in Fig. 5) while the western portion stalled just south of

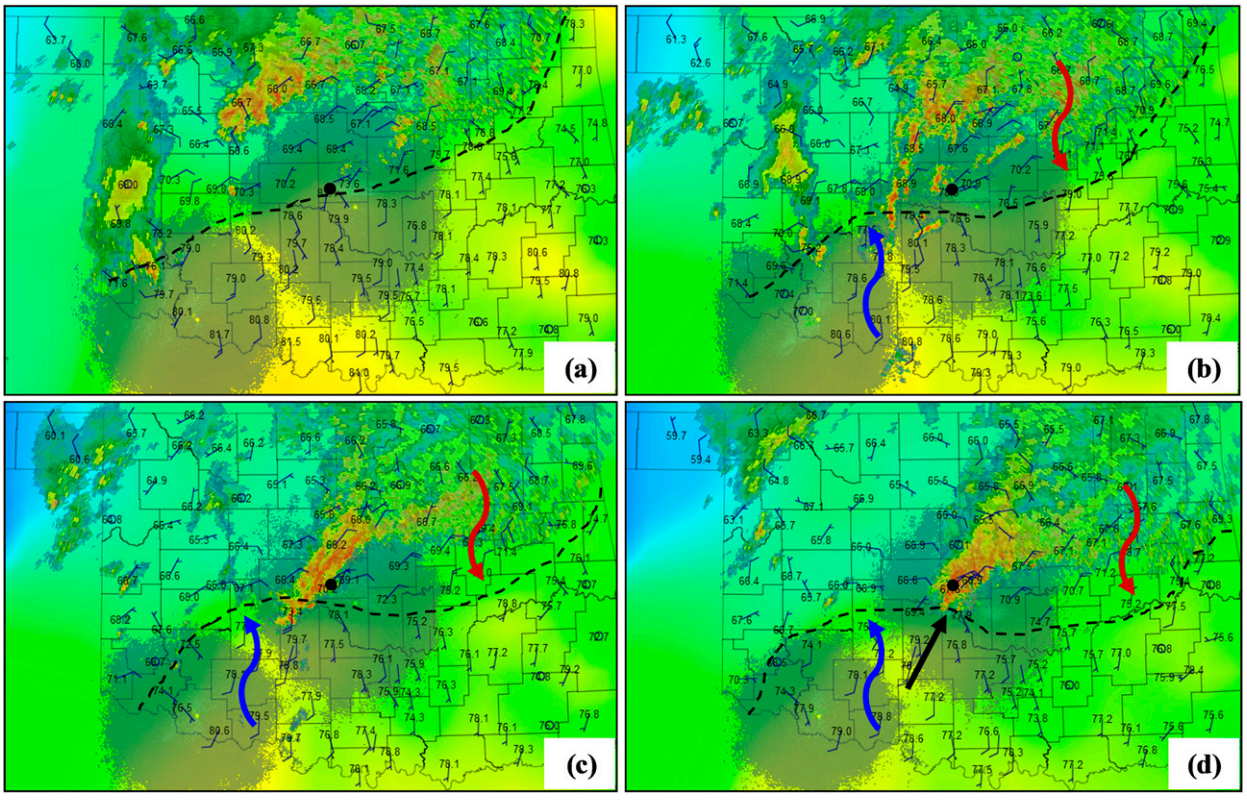

FIG. 5. As in Fig. 4, but valid at (a) 0730, (b) 0830, (c) 0930, and (d) 1030 UTC. Red arrows highlight the advancing segment of the outflow boundary, blue arrows highlight the stalled segment of the outflow boundary, and the black arrow approximates the direction of the low-level jet.

Oklahoma City (blue arrows). This along-line variation reoriented that segment of the outflow boundary to a direction almost perpendicular to the low-level jet (black solid arrow in Fig. 5d, approximated from the 1200 UTC OUN sounding). As a result, a corridor of moist, uncapped, conditionally unstable air underwent strong isentropic ascent directly upstream from Oklahoma City.

WSR-88D scans from 0830 to 1030 UTC (Figs. 5b–d) showed isolated convective cells forming near the region of strong ascent and rapidly intensifying as they approached Oklahoma City, organizing into a small but vigorous backbuilding/quasi-stationary MCS instead of the training line/adjacent stratiform MCS type (Schumacher and Johnson 2005) predicted by the Maddox et al. (1979) model for mesohigh events. The vector addition method described in Corfidi et al. (1996) was used to estimate the predicted motion of the MCS core; the advection vector was estimated as a simple layer average of the mean 850–300-hPa wind from the 1200 UTC OUN sounding (17.2 m s^{-1} from 224°), while the propagation vector was estimated as the negative of the 850-hPa wind (19.5 m s^{-1} from 40°). The sum of the two vectors gives a predicted MCS motion of 2.6 m s^{-1} from 15°. Thus, rather than moving over the cold pool and losing intensity, this new MCS remained largely in phase with the outflow boundary (with both moving very slowly) for several hours; this appears to have further intensified the new cells building on the southwest (upstream) side of the MCS. As a result, mesonet sites in the Oklahoma City area recorded average rainfall rates of over 25 mm h^{-1} for the 6-h period from 0900 to 1500 UTC (Fig. 6).

This observational analysis highlights features that appeared to substantially influence the development of heavy precipitation in central Oklahoma on 14 June. However, it does not establish their relative importance or the factors that determined the manner in which they evolved. The CAPS SSEF output for this event is now examined, both to identify the most important aspects of the numerical model for producing a successful forecast for the event and to explain the observed evolution of those features.

3. Data and methods

a. *CAPS SSEF description*

Since 2007, CAPS has been producing experimental convection-permitting/convection-resolving resolution

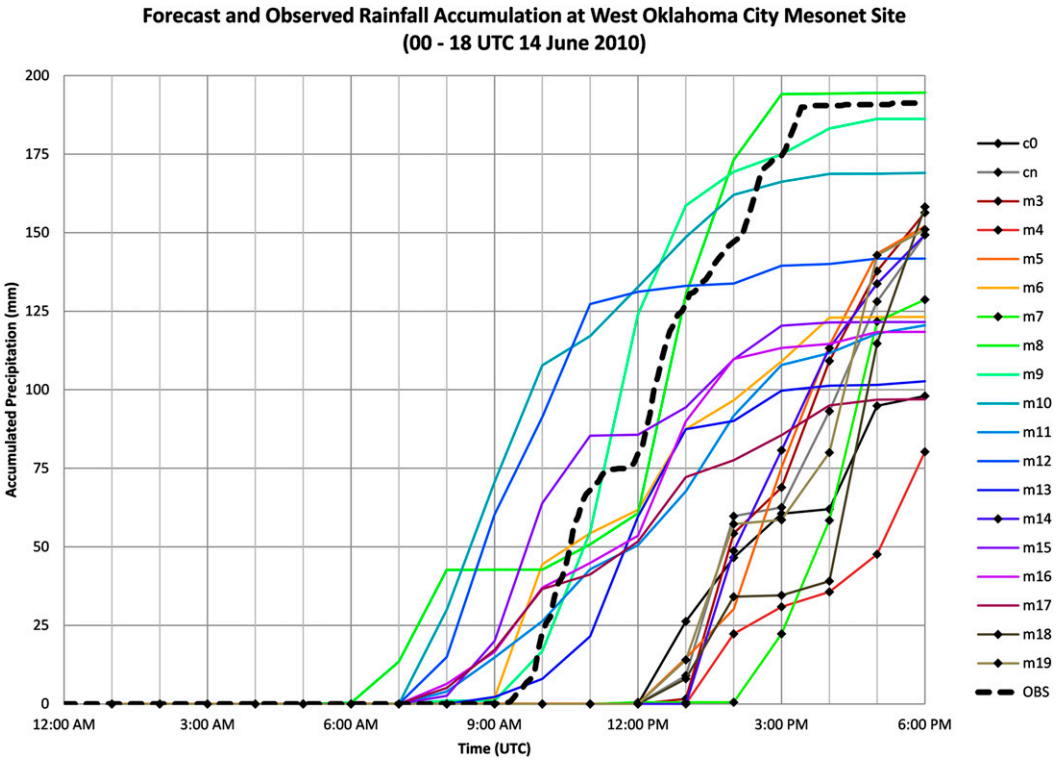

FIG. 6. Observed 14 Jun 2010 rainfall accumulation at the West OKC (OKCW) Mesonet site (black dashed line) along with maximum forecast rainfall accumulation within a 25-km radius of the site for SSEF ARW members (with diamonds denoting members employing Thompson microphysics) vs time (UTC).

real-time ensemble forecasts covering the continental United States (CONUS; e.g., Xue et al. 2007, 2009), as part of the NOAA HWT Spring Experiment (Clark et al. 2012). Starting in 2009, the CAPS SSEF included members using the ARW, WRF-NMM, and the ARPS dynamic cores and were run over a full CONUS domain at 4-km grid spacing (Xue et al. 2010), a resolution that is considered to be convection permitting (Bryan et al. 2003). In addition, a 1-km grid spacing forecast using the ARW with the same configuration as the control members of the SSEF was also run to examine the impact of grid resolution (Xue et al. 2013). For the spring of 2010, the CAPS ensemble consisted of 19 ARW members, 5 WRF-NMM members, and 2 ARPS members. All of these members except for one for each dynamic core included the assimilation of radial velocity and reflectivity data from all WSR-88D radars in their initial conditions at 0000 UTC. The non-radar-assimilating members used the North American Mesoscale Forecast System (NAM) 0000 UTC analysis directly as the initial conditions. The data assimilation used the ARPS three-dimensional variational data assimilation (3DVAR)/cloud analysis system (Xue et al. 2003; Hu et al. 2006), and in addition to the radar data, wind profiler, Surface Aviation Observation (SAO), and Oklahoma Mesonet observations were also analyzed by the ARPS 3DVAR, and the 0000 UTC NAM analysis was used as the background. Additional details on the assimilation procedure can be found in Xue et al. (2009).

Variations in the model configurations in an ensemble are often used to account for model prediction uncertainties and to allow the ensemble to capture multiple convective modes in a given forecast period. This is especially important when model errors, such as those associated with the parameterization of microphysical and boundary layer processes, are significant. For example, while Dawson et al. (2010) found that single-moment bulk microphysics schemes tended to overpredict the cold pool strength and extent for tornadic supercells, Bryan and Morrison (2012) and Clark et al. (2012) found that double-moment schemes operating at convection-allowing resolutions may overpredict stratiform precipitation in squall lines. Therefore, along with perturbations applied to the initial and boundary conditions, the CAPS SSEF is populated by varying the combination of parameterizations for land surface

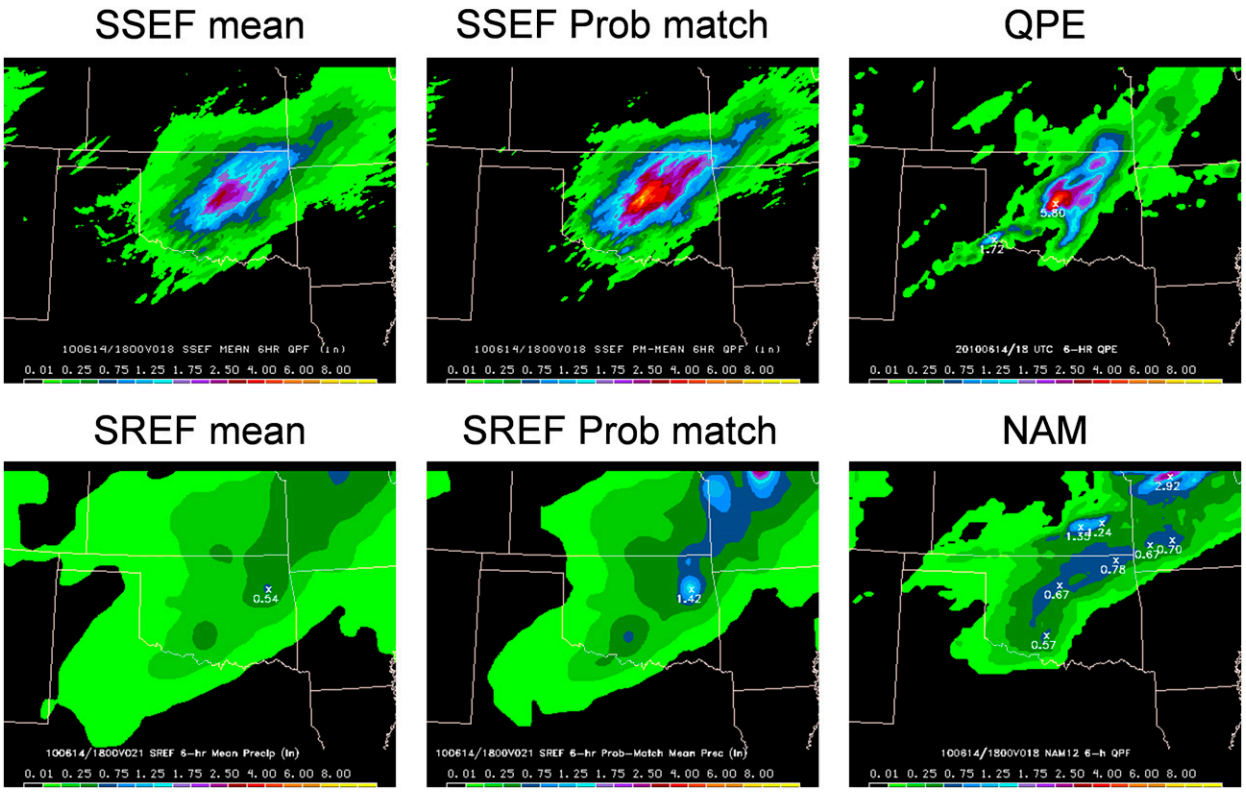

FIG. 7. Various representations of 6-h accumulated precipitation valid 1800 UTC 14 Jun 2010. (left) The CAPS SSEF and NCEP SREF ensemble means, (middle) the corresponding probability-matched ensemble means, and (right) the stage IV observed precipitation analysis and NCEP NAM forecast. [Taken from Xue et al. (2010, Fig. 6).]

interaction, boundary layer turbulence, radiative transfer, and microphysics. The configurations employed in the 2010 SSEF members are summarized in Tables 1–3 of Xue et al. (2010).

Fields for a variety of diagnostic parameters and forecast variables, including reflectivity and accumulated precipitation, were processed from the SSEF output and made available to the HWT in real time. Along with the ensemble mean and maximum, the neighborhood probability and probability-matched mean of hourly accumulated precipitation and reflectivity were computed to circumvent the ''smearing'' effect of simple ensemble averaging (Xue et al. 2010). Ebert (2001) found that probability matching improved forecast skill for a ''poor man's ensemble'' of seven operational NWP models, and Xue et al. (2010) likewise found it to be superior for predicting heavier rains during the Spring Experiment (Fig. 1 in Xue et al. 2010). In particular, the probability-matched mean QPF from the SSEF improved substantially on the operational NCEP NAM or Short-Range Ensemble Forecast (SREF) forecasts for the June 14 Oklahoma City flooding event (Fig. 7).

b. *Statistical and qualitative analysis procedure*

The three-dimensional forecast states and various two-dimensional forecast (e.g., accumulated precipitation) and diagnostic (e.g., updraft helicity) fields for the CAPS SSEF members were saved at hourly intervals. For the purpose of this study, comparing results from different dynamic cores is complicated by model configuration; none of the ARPS or WRF-NMM members employed the same combination of microphysics, radiative transfer, boundary layer, and land surface parameterizations as any of the ARW members, and therefore it would be difficult to determine which differences in output are due to choices of parameterizations and which are due to fundamental differences among ARW, WRF-NMM, and ARPS. To avoid this issue, and because the number of ARW members is deemed to be sufficient for our purpose, only the ARW members are analyzed here.

The QPF skill of each ARW member was evaluated using stage IV hourly accumulated precipitation analyses produced by the National Centers for Environmental Prediction (Lin and Mitchell 2005). Those data

have approximately 4-km resolution. Generally, calculation of skill at forecasting precipitation at a given threshold is accomplished via a contingency table in which the following events are counted:

- hit (both the forecast and the observation meets the threshold),
- miss (the observation meets the threshold but the forecast does not),
- false alarm (the forecast meets the threshold but the observation does not), and
- correct negative (neither the forecast nor the observation meets the threshold).

As noted in Clark et al. (2010a), simple point-by-point verification of a precipitation forecast is not a good indicator of high-resolution model forecast skill since small spatial errors incur large penalties, particularly for intense precipitation. For this reason, a neighborhood-based verification approach similar to theirs was employed here. In this approach, correct negatives are assessed point by point while hits, misses, and false alarms are assessed using a specified neighborhood radius. This method evaluates skill in a more realistic way by not penalizing a forecast that correctly predicts intense rainfall (while erring slightly in location) more than one that misses the forecast entirely. To use this method, the forecast and observation locations must be collocated. To accomplish this, the gridded hourly precipitation accumulations from the 18-h period encompassing the event (i.e., from 0000 to 1800 UTC) for each ARW member were mapped to the stage IV grid locations using bilinear interpolation.

To obtain an initial overview of QPF skill, equitable threat scores (ETSs) were calculated using hourly accumulation thresholds of both 10 and 20 mm along with a neighborhood radius of 25 km over the domain illustrated in Fig. 8 for the period from 0000 to 1800 UTC. This region was selected to account for possible influences from features of varying convective intensities near the early MCS in northwest Oklahoma, the later MCS in central Oklahoma, and the warm region in southern Oklahoma. To focus on the MCS itself, additional ''event intensive'' threat scores were calculated for selected members within region C for the period from 0800 to 1500 UTC. (The rationale for selecting those members is described in section 4c.)

Along with QPF evaluation, high-resolution verification of forecast surface conditions was performed using observations from the Oklahoma Mesonet. The actual position of the outflow boundary over western Oklahoma from 0500 to 1400 UTC was analyzed by mapping the mesonet temperature observations to the ARW grid using a two-pass Barnes analysis. To remove the impacts

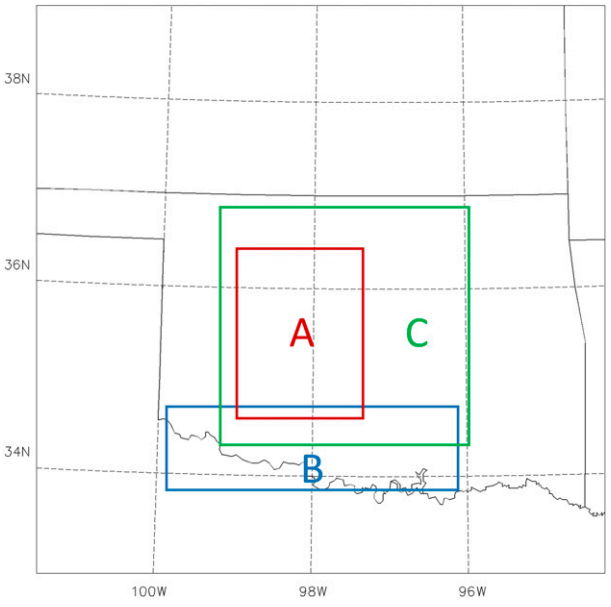

FIG. 8. Region of the ARW model output used for initial QPF ETS calculations, along with regions used for outflow boundary verification (red), verification of surface and upper-air conditions (blue), and event-intensive ETS calculations (green). Latitude and longitude coordinates are given along the axes.

of isolated warm-region convection, a top-hat filter with a 25-km radius was applied to the results of the Barnes analyses. Manual examination of the smoothed fields indicated that the 70°F isotherm provided a reasonable approximation for the actual outflow boundary position in the region of interest (i.e., region A in Fig. 8) throughout the forecast period, while the 72°F isotherm provided a better approximation for the outflow boundary positions from each of the ARW members (suggesting persistent warm bias near the boundary). Then, using prior knowledge that both the observed and forecast outflow boundaries had a generally east–west orientation in region A, outflow boundary positions were estimated by searching for the northernmost instance of temperature above the selected threshold along each meridional slice in region A of the ARW grid. The line-averaged bias and root-mean-square error (RMSE) in north–south boundary position were then computed at hourly intervals.

Additionally, the forecast 2-m temperature and dewpoint fields were interpolated to the mesonet station locations within the area designated as region B in Fig. 8 and used to calculate the warm-region bias and root-mean-square error at hourly intervals for each of the ARW members. Simple bivariate correlations between QPF skill and these aspects of the low-level forecasts were assessed using Pearson correlation coefficients r. A similar process was then used to search for correlations

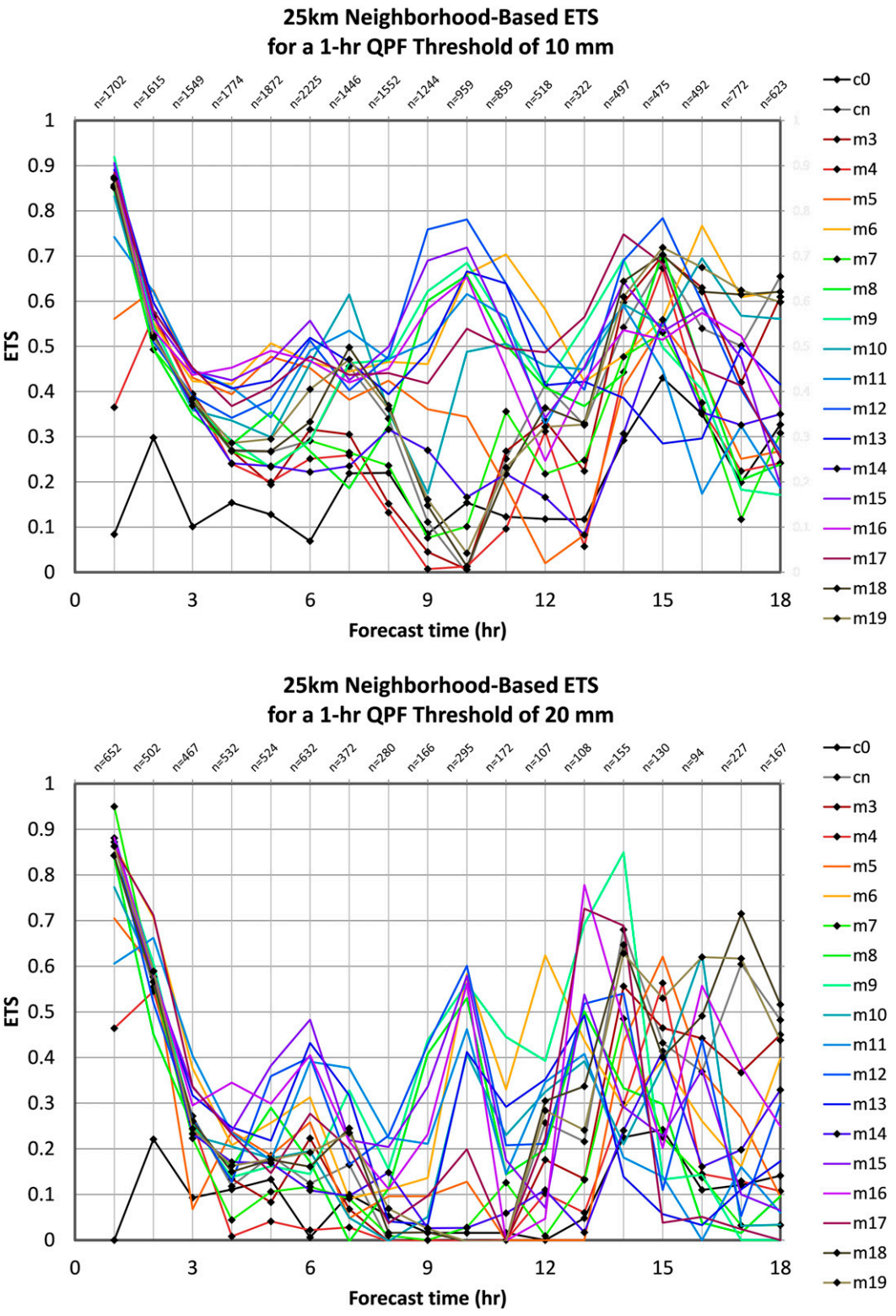

FIG. 9. Hourly QPF threat scores for the full domain shown in Fig. 8 using hourly accumulation thresholds of (top) 10 and (bottom) 20 mm, with SSEF members designated as in Fig. 6.

TABLE 1. ARW members ranked by 10 mm h^{-1} QPF ETS aggregated from 0000 to 1800 UTC 14 Jun 2010 for the full domain in Fig. 8. Characteristics of each member are listed at right. PBL schemes include the Mellor–Yamada–Nakanishi–Niino (MYNN) and the quasi-normal scale elimination (QNSE) schemes. More details can be found in Xue et al. (2010).

Rank	Member	ETS	Microphysics	PBL	LSM	Initial conditions	Boundary conditions
1	m15	0.5243	WDM6	MYJ	Noah	0000 UTC ARPSa	0000 UTC NAMf
2	m6	0.5223	Morrison	YSU	RUC	cn − em-p1_pert	2100 UTC SREF em-p1
3	m12	0.5192	WDM6	QNSE	RUC	cn + etaKF-p1_pert	2100 UTC SREF etaKF-p1
4	m16	0.4904	WSM6	MYJ	Noah	0000 UTC ARPSa	0000 UTC NAMf
5	m17	0.4852	Morrison	MYJ	Noah	0000 UTC ARPSa	0000 UTC NAMf
6	m13	0.4837	WSM6	QNSE	Noah	cn − etaBMJ-n1_pert	2100 UTC SREF etaBMJ-n1
7	m11	0.4701	Ferrier	YSU	Noah	cn − etaKF-n1_pert	2100 UTC SREF etaKF-n1
8	m9	0.4553	WDM6	MYNN	Noah	cn + nmm-p2_pert	2100 UTC SREF nmm-p2
9	m10	0.4438	Ferrier	YSU	RUC	cn + rsmSAS-n1_pert	2100 UTC SREF rsmSAS-n1_pt
10	m8	0.4175	WSM6	QNSE	RUC	cn − nmm-p1_pert	2100 UTC SREF nmm-p1
11	m19	0.4043	Thompson	MYNN	Noah	0000 UTC ARPSa	0000 UTC NAMf
12	m18	0.3933	Thompson	QNSE	Noah	0000 UTC ARPSa	0000 UTC NAMf
13	m5	0.3867	Morrison	YSU	RUC	cn + em-p1 + recur pert	2100 UTC SREF em-p1
14	cn	0.3766	Thompson	MYJ	Noah	0000 UTC ARPSa	0000 UTC NAMf
15	m3	0.3428	Thompson	MYJ	Noah	cn + random pert	0000 UTC NAMf
16	m7	0.3069	Thompson	QNSE	Noah	cn + em-p2_pert	2100 UTC SREF em-p2
17	m14	0.3062	Thompson	MYNN	RUC	cn + etaBMJ-p1_pert	2100 UTC SREF etaBMJ-p1
18	m4	0.2632	Thompson	MYJ	Noah	cn + RF-smoothed pert	0000 UTC NAMf
19	c0	0.1944	Thompson	MYJ	Noah	0000 UTC ARPSa	0000 UTC NAMf

between QPF skill and model depiction of the upper-air conditions highlighted in section 2 (e.g., magnitudes of MUCAPE and MUCINH; strength of the low-level jet) in region B. Finally, after the influence of model settings on these metrics was inferred and members suffering from systemic errors were discarded, the remaining members were qualitatively compared in hopes of identifying specific phenomena associated with subsequent high forecast skill in order to better understand the processes responsible for the heavy rains observed in this event.

4. Results and discussion

a. *Statistical relationships between QPF skill and low-level conditions*

The hourly QPF threat scores at thresholds of 10 and 20 mm are plotted in Fig. 9, while the accumulated 10-mm threat scores from 0000 to 1800 UTC are ranked in Table 1. First, both the plots and the ranked scores make it clear that the performance of the control ARW member with no radar data assimilation (c0) is the worst, remaining at or near the bottom of the ensemble envelope for the entire period. The importance of the radar data assimilation is illustrated by comparing the simulated reflectivity of the two control members (c0 and cn) without and with the assimilation of radar data. Figure 10 shows that without the assimilation of radar data in the initial conditions at 0000 UTC, c0 is much too slow in developing organized convection and a subsequent cold pool. (The stronger cold pool in member cn is inferred from the more developed reflectivity signature of the convective cluster in Fig. 10e compared with Fig. 10h, including an extensive region of stratiform precipitation behind the intense cells on the leading edge.) As detailed in the event synopsis, the cold pool from the earlier convection appears to have been a crucial component in the subsequent development of precipitation throughout the region shown in Fig. 8. Therefore, the negative impact of this initial error is evident throughout the forecast period, although it diminishes after the first 6 h (falling within the ensemble envelope, albeit persistently on the low side) in general agreement with the results of Stratman et al. (2013).

When examining the SSEF member attributes in Table 1 further, the most obvious pattern is the predominance of the Thompson microphysics scheme (Thompson et al. 2004) in the lower-scoring members, regardless of other model attributes; eight of the nine lowest rankings are occupied by the members that used the Thompson scheme. (The exception, m5, will be examined later.) Those members are denoted by diamond markings in Fig. 9; their comparative lack of skill is concentrated in the period from 0800 to 1300 UTC (i.e., from 8 to 13 h after initialization), and it is clear from Fig. 6 that this error stems from a late bias of several hours in the forecasted onset of precipitation in the Oklahoma City area.

The mean hourly line-averaged errors and RMS errors in outflow boundary position from 05 to 1400 UTC for region A are shown in Fig. 11. Since the outflow

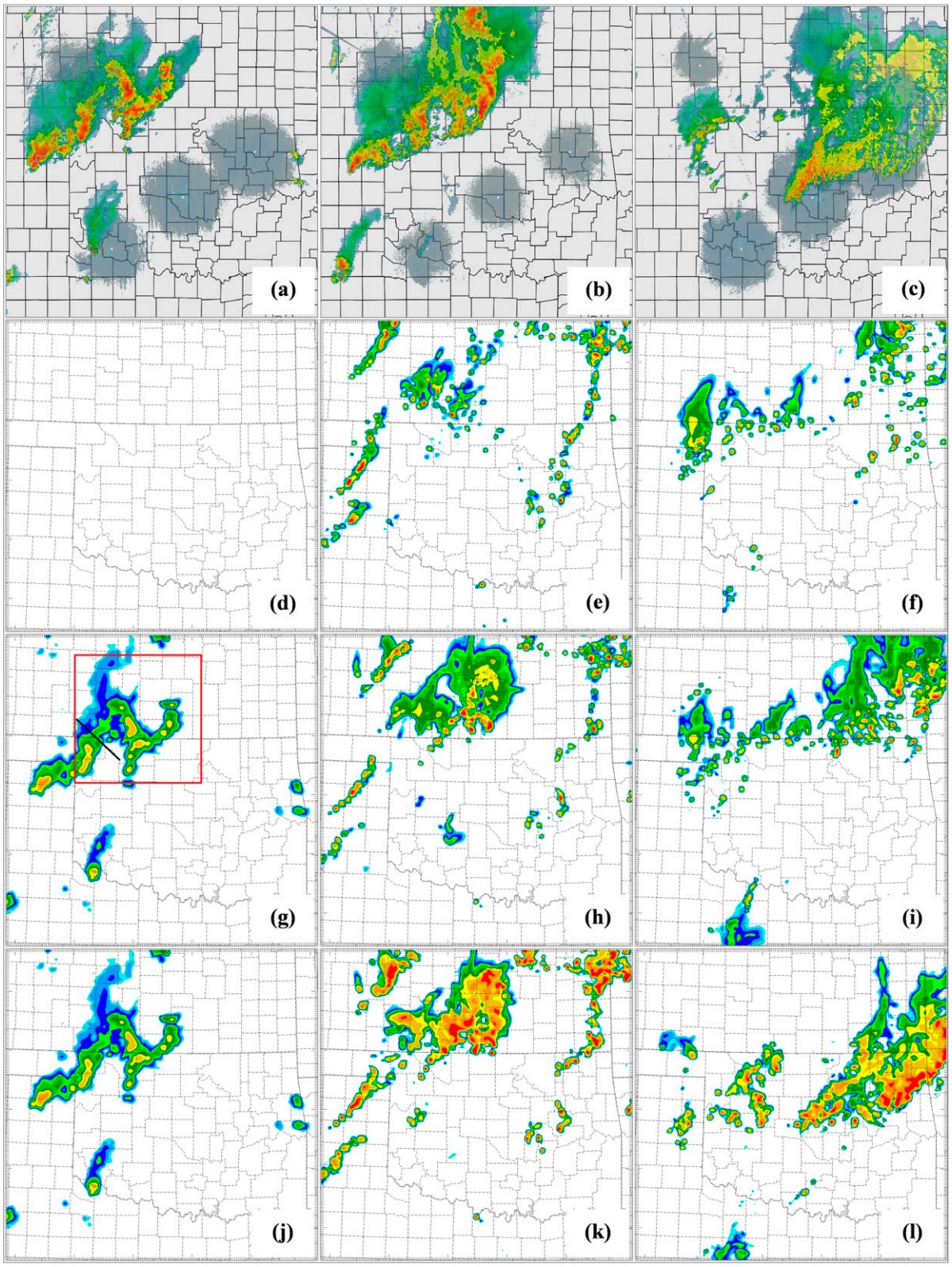

FIG. 10. (a)–(c) Observed and simulated radar reflectivity from ARW members (d)–(f) cn without radar data assimilation, (g)–(i) c0 with radar data assimilation, and (j)–(l) m15 with WDM6 microphysics valid at (from left to right) 0100, 0200, and 1000 UTC 14 Jun. The solid black line in (g) is the position of the vertical cross section used for Fig. 12, while the red box shows the region plotted in Fig. 13.

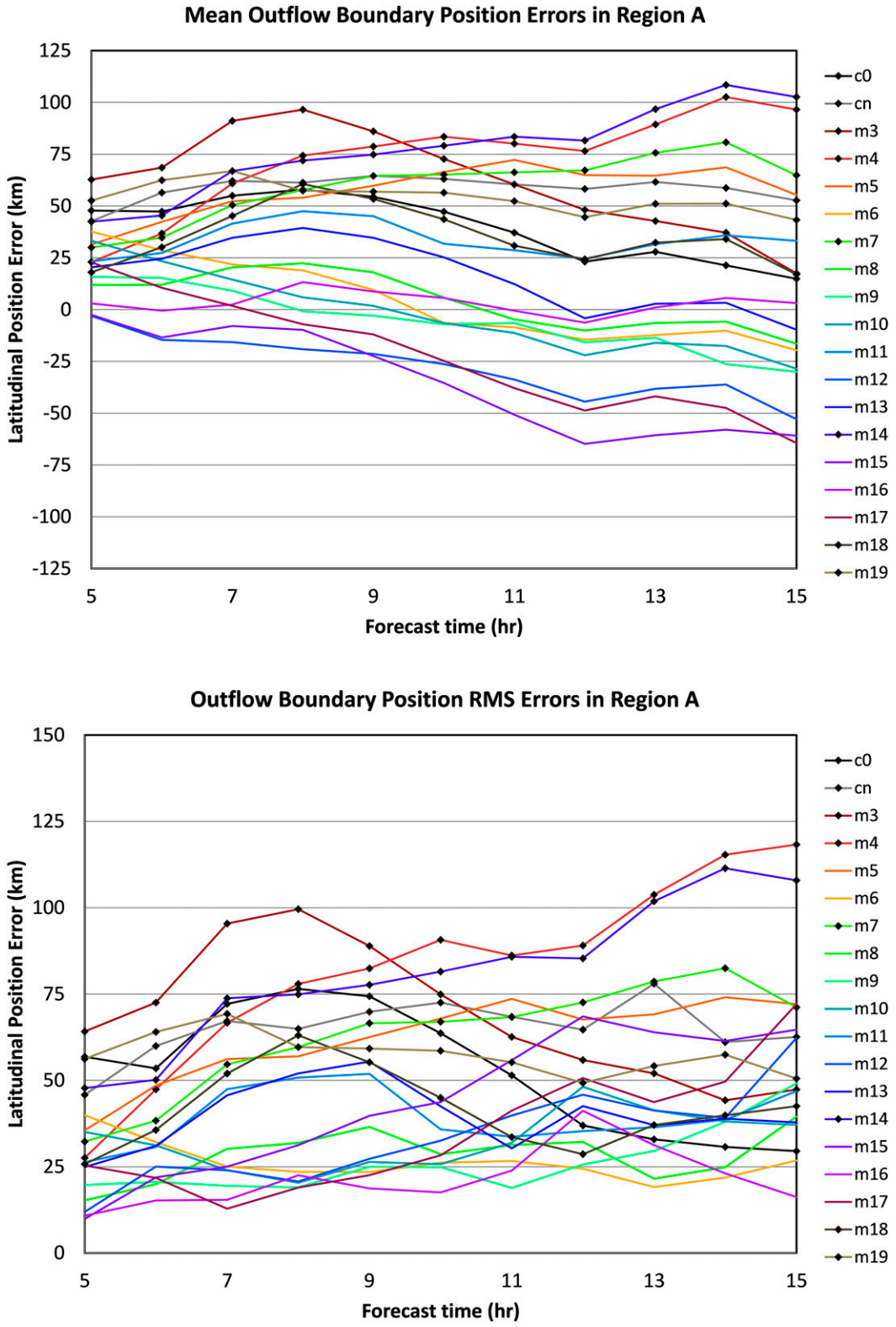

FIG. 11. (top) Hourly line-averaged errors and (bottom) hourly RMS errors in north–south positions of the forecast outflow boundaries in region A, with SSEF members designated as in Fig. 6.

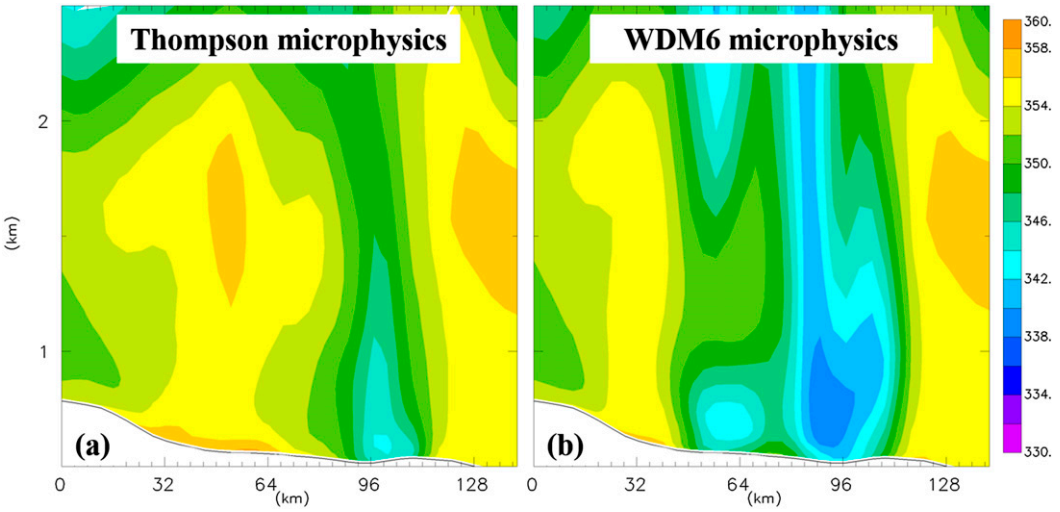

FIG. 12. Vertical cross section of equivalent potential temperature taken along the black line in Fig. 10g for (a) cn and (b) m15 members 1 h after initialization.

boundary generally moved southward in this area, positive position errors indicate the boundary moving too slowly, which clearly predominates in the members that used the Thompson scheme. The RMS errors for the Thompson scheme members are greater on average as well (although the difference gradually becomes less noticeable after 1000 UTC as the stationary boundary becomes active in those members and pushes into western Oklahoma as a cold front). Reviewing the member attributes in Table 1, a direct illustration of the impact of the Thompson scheme on initial cold pool development is obtained by comparing the forecasts of members cn and m15. Experiment m15 is a physics sensitivity member that only differs from cn in the microphysics scheme used; the former uses the Thompson scheme while the latter uses the six-species double-moment WRF, or WDM6, scheme described by Lim and Hong (2010). Since the setups for the two members are otherwise identical, any short-term differences in model output may confidently be attributed to differences in model microphysics.

Figure 12 indicates that the Thompson treatment of evaporative cooling and cold pool development for the initial convection in northwest Oklahoma differs markedly from that of the WDM6 scheme within the first hour of the model forecast; from vertical cross sections taken at the location of the black line in Fig. 10g for both members, it is clear that the WDM6 cold pool is deeper, broader, and characterized by lower equivalent potential temperature. Furthermore, Fig. 13 shows that the Thompson scheme produces a greater amount of vertically integrated cloud water and substantially less vertically integrated rainwater (in terms of both magnitude and spatial extent) in conjunction with the early convection than the WDM6 scheme does. The integrated snow content is also much greater for the Thompson scheme than for the WDM6 scheme, in some places by a factor of 5 or more (not shown); this enhanced snow production relative to other schemes has been noted in other warm-season convection modeling studies (e.g., Powell et al. 2012; Wheatley et al. 2014).

Intensive investigation of the reasons for these microphysical differences would require rerunning the ensemble to obtain output at greater than hourly resolution, which is beyond the scope of this paper. As it stands, these facts suggest that the Thompson scheme's treatment of the rainwater drop size distribution and the concentration of activated cloud condensation nuclei (see Thompson et al. 2004) may favor lower autoconversion rates and reduced collision/coalescence efficiency within the initial convective cells. This would leave more condensate in the form of cloud water and reduced rainwater at lower levels in the Thompson case, which in turn would lead to weaker cold pool development as well as a greater amount of water vapor being converted to snow aloft. In any case, the initial weakness of the cold pool in the Thompson member results in substantial errors in both the timing and the mode of the later precipitation in central Oklahoma (see Figs. 10c,i,l).

The large ensemble spread in outflow boundary positions becomes the dominant factor in the temperature and dewpoint variations in region B after 1200 UTC. Also, autocorrelation calculations indicate that the hourly QPF skill scores for a given member must be

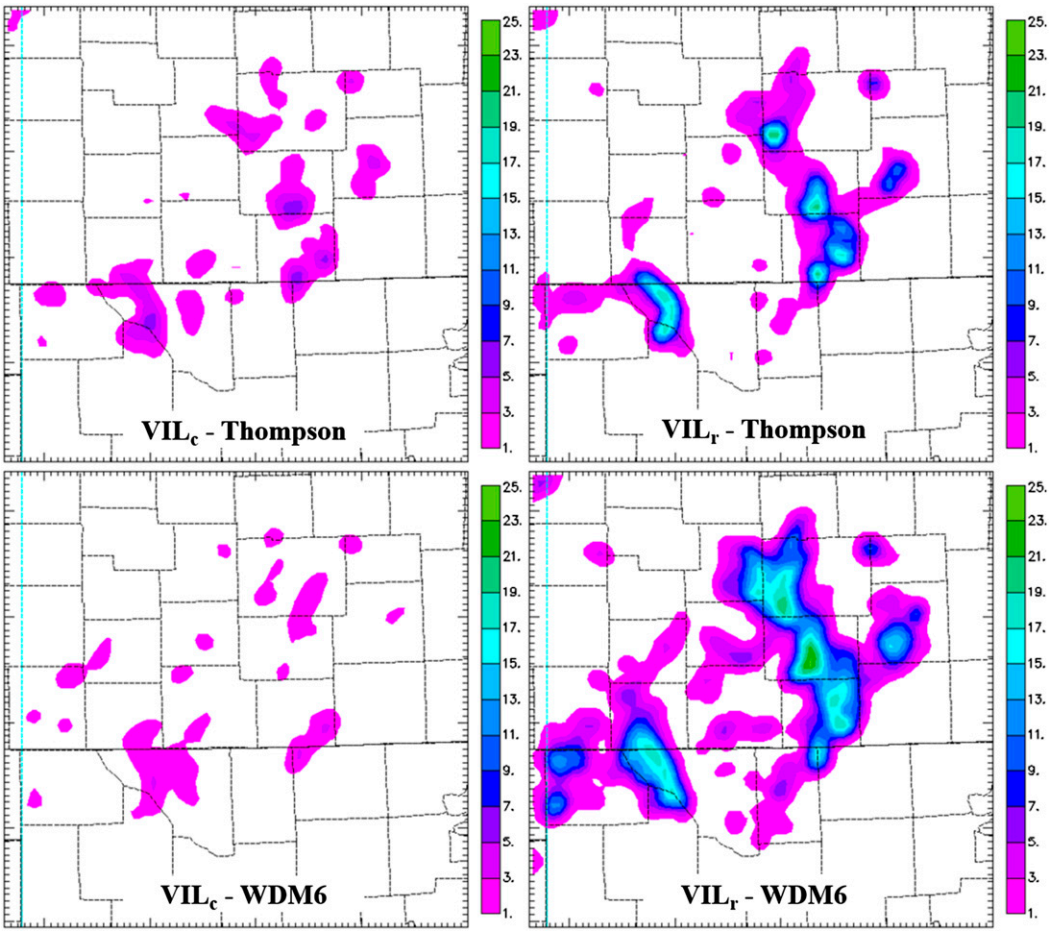

FIG. 13. (left) Vertically integrated cloud water (VIL$_c$; kg m^{-2}) and (right) vertically integrated rainwater content (VIL$_r$; kg m^{-2}) predicted by members (top) cn and (bottom) m15 at 0100 UTC in the region marked by the red box in Fig. 10g.

sampled at least 2 h apart in order for consecutive data points to be considered statistically independent. Therefore, the conditions for each member were sampled every 2 h from 0600 to 1200 UTC, giving $n = 76$ for the QPF skill correlation calculations. Since some delay is expected between the observed or modeled conditions in southern Oklahoma and any impacts on precipitation farther north, correlations were also calculated using varying lag times between the region B samples and the hourly QPF skill scores. The highest correlations (which generally resulted from a 2-h lag) are shown here.

Figure 14 shows that the choices of planetary boundary layer (PBL) scheme and land surface model (LSM) influence the forecast surface conditions [e.g., with comparatively warmer and drier conditions from the Yonsei University (YSU) scheme after a few hours, corroborating the results in Hu et al. (2010)]. However, Table 2 indicates that these variations do not significantly influence QPF skill for this event, while the outflow boundary position bias and RMSE are strongly correlated with QPF skill. To check this result, correlations with 3-h QPF skill using accumulation thresholds of 10 and 30 mm were also calculated for the surface forecast errors in region B. However, the results did not generally improve upon those obtained from 1-h QPF skill and are not shown here.

b. *Statistical analysis relating upper-air conditions to QPF skill*

The sounding in Fig. 3b depicts four key features associated with the event: a low-level jet with a strong meridional component, exceptionally high precipitable water content, substantial MUCAPE, and a lack of MUCINH. For the low-level jet, the ensemble member depictions of the average meridional 850-hPa wind speed in region B were investigated. Small systemic differences are suggested by the plots in Fig. 14 (e.g., a slightly reduced diurnal cycle for the low-level jet from

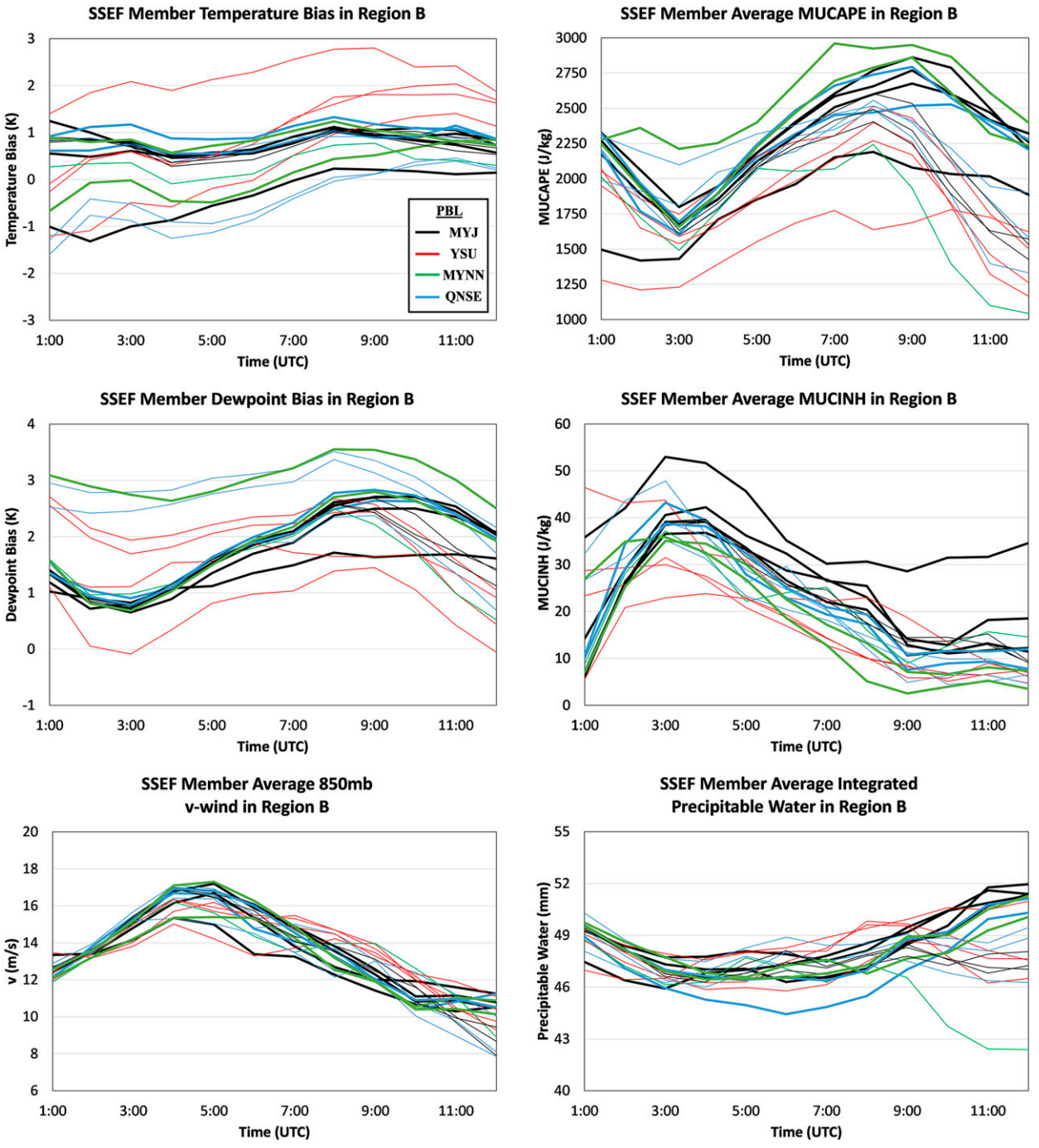

FIG. 14. Hourly temperature bias (K), average MUCAPE (J kg^{-1}), dewpoint bias (K), average MUCINH (J kg^{-1}), average 850 hPa meridional wind speed (m s^{-1}), and average precipitable water (kg m^{-2}) in region B of Fig. 8. Members using the Noah LSM scheme are plotted in boldface.

the YSU PBL members; a stronger nocturnal jet from the Noah LSM members). However, the correlation between these differences and variations in subsequent QPF skill appears to be dubious, with $r = 0.00$ for the 10-mm threshold and -0.21 for the 20-mm threshold.

Variations in forecast precipitable water ($r = -0.30$ for the 10-mm threshold and -0.27 for the 20-mm threshold), MUCAPE ($r = -0.30$ for 10 mm and -0.61 for 20 mm), and MUCINH ($r = -0.25$ for 10 mm and -0.33 for 20 mm) show a somewhat higher correlation with

TABLE 2. Pearson correlation coefficients relating surface forecast skill metrics to QPF forecast skill for the period from 0600 to 1200 UTC 14 Jun 2010.

Parameter	*r* (10-mm 1-h QPF)	*r* (20-mm 1-h QPF)
Temp bias	0.10	0.09
Temp RMSE	0.13	0.12
Dewpoint bias	−0.04	−0.26
Dewpoint RMSE	0.02	−0.20
Outflow boundary position bias	−0.74	−0.57
Outflow boundary position RMSE	−0.74	−0.60

forecast skill. However, Fig. 14 does not show a discernible pattern linking the PBL or the LSM scheme to forecast precipitable water, and while relationships between those settings and MUCAPE and MUCINH are more strongly suggested, the general implications for QPF skill are unclear. For example, the YSU members generally have less MUCAPE (as might be expected from the impacts on surface temperature and dewpoint noted earlier) and less MUCINH in the hours immediately preceding the event; however, there is no prevalence of YSU members in the skill rankings in Table 1. Furthermore, the scatterplots in Fig. 15 emphasize that variations in MUCAPE, MUCINH, and precipitable water are not as strongly correlated to QPF skill as variations in outflow boundary position.

Figure 14 also shows clear stable outliers in terms of MUCAPE and MUCINH, corresponding to members m4 (black outlier line in the top-right panel) and m5 (red

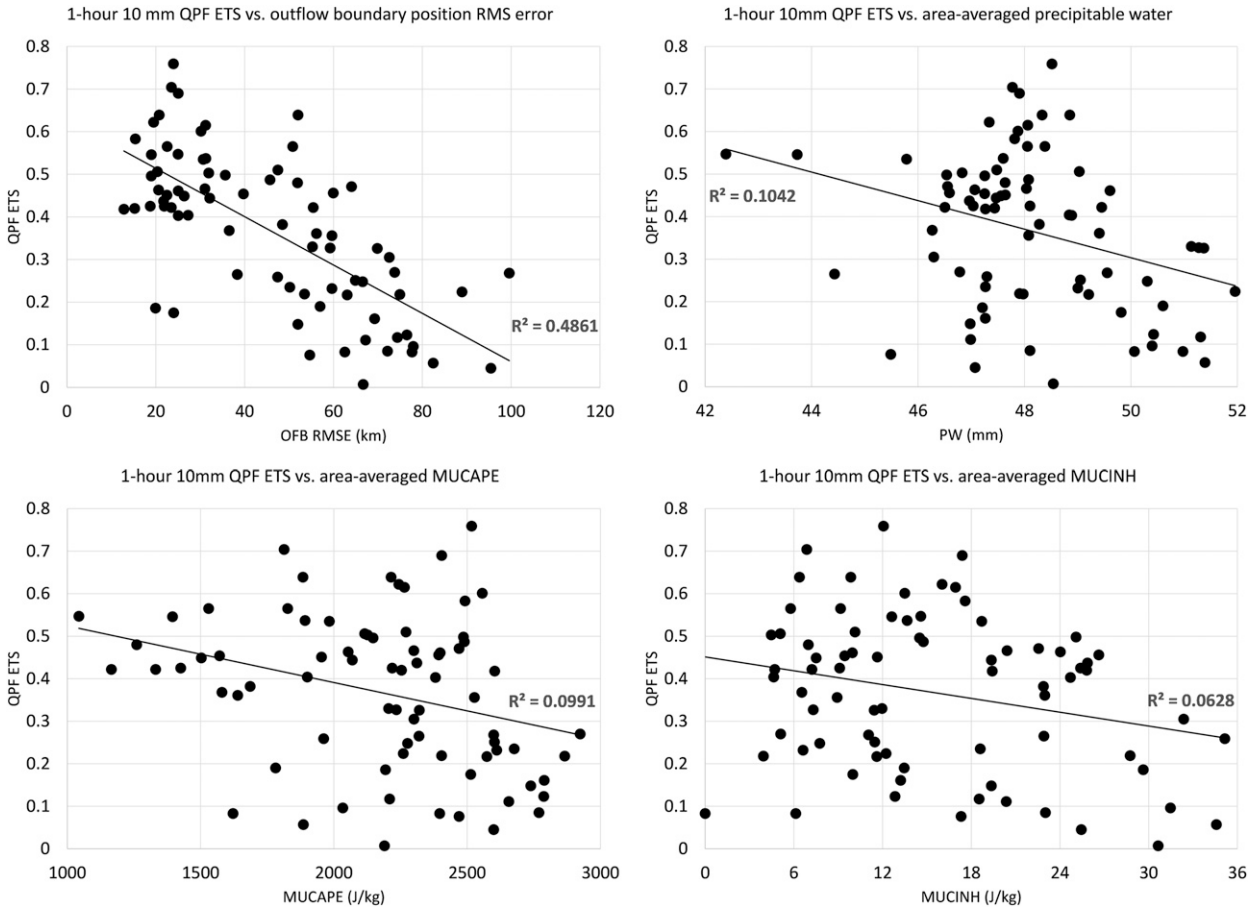

FIG. 15. Scatterplots and trend lines for 1-h ensemble member QPF skill using a 10-mm accumulation threshold, sampled every 2 h for the period from 0600 to 1200 UTC, as a function of (a) outflow boundary position RMS error (km) in region A and (b) vertically integrated precipitable water (mm), (c) MUCAPE (J kg^{-1}), and (d) MUCINH (J kg^{-1}) averaged over region B in Fig. 8.

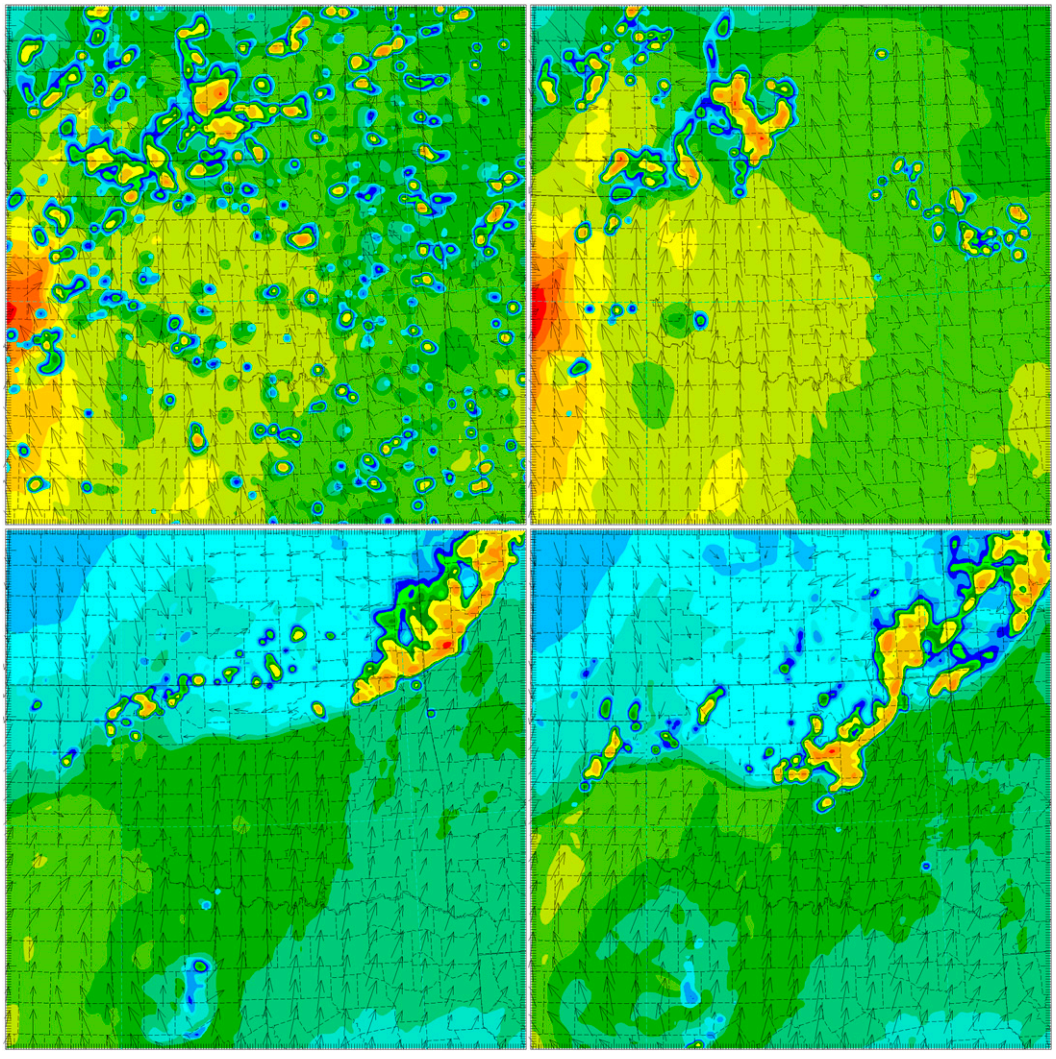

FIG. 16. Simulated near-surface reflectivity and wind vectors overlaid on surface potential temperature at (top) 0100 and (bottom) 0900 UTC for members (left) m5 and (right) m6. These two members are the same except for the inclusion of additional convective perturbations in the initial conditions in m5.

outlier line in the center-right panel), respectively. Reviewing Table 1, this appears to stem from the inclusion of convective-scale perturbations (denoted "recur pert" for m4 and "RF-smoothed pert" for m5, with spatial decorrelation scales of 12 and 3 km in the horizontal and vertical, respectively) in the temperature and moisture fields of the initial conditions for those members; as shown in Fig. 16, these perturbations initiate widespread spurious convection in the domain that persists for a few hours in some areas, artificially stabilizing the atmosphere and contributing to later errors in outflow boundary location similar to those seen in the members that employed Thompson microphysics. The negative effects of these perturbations are also noted in Johnson et al. (2014); for these perturbations to contribute positively to the ensemble spread and ensemble forecast perturbations, the magnitudes of such perturbations need to be tuned.

c. *Qualitative high-rank/low-rank comparison of convective features*

The preceding quantitative analysis highlights the importance of the outflow boundary and indicates that predictions of its behavior are strongly influenced by model microphysics in the present case. However, it does not provide much insight into the physical causes of the observed outflow boundary evolution. Furthermore, because it only considers parameters averaged over a relatively large area, it does not consider the potential roles played by more localized features or by the

TABLE 3. ARW members ranked by 20 mm h^{-1} QPF ETS aggregated from 0800 to 1500 UTC in region C of Fig. 8. Model settings and previous rank (from Table 1) are listed at right.

Rank	Member	ETS	Microphysics	PBL	LSM	Previous rank
1	m9	0.614	WDM6	MYNN	Noah	8
2	m12	0.567	WDM6	QNSE	RUC	3
3	m6	0.559	Morrison	YSU	RUC	2
4	m10	0.488	Ferrier	YSU	RUC	9
5	m8	0.484	WSM6	QNSE	RUC	10
6	m16	0.475	WSM6	MYJ	Noah	4
7	m15	0.463	WDM6	MYJ	Noah	1
8	m13	0.433	WSM6	QNSE	Noah	6
9	m11	0.288	Ferrier	YSU	Noah	7
10	m17	0.286	Morrison	MYJ	Noah	5

environment outside the averaging area. These questions are now addressed through a directed qualitative examination of the forecast fields.

Since the progress of the outflow boundary has the strongest correlation with QPF skill, and since the members that used the Thompson microphysics scheme and/or convective-scale perturbations for the initial conditions are poorer at predicting outflow boundary positions, those members were eliminated from further analysis. As shown in Fig. 6, the remaining 10 members produced reasonable predictions for the timing of the event as well as the intensity (particularly in the period prior to 1200 UTC) and thus contributed positively to the ensemble forecast. To focus on the smaller variations among those members, QPF skill was recalculated in region C of Fig. 8 for the period from 0800 to 1500 UTC using a 1-h accumulation threshold of 20 mm. The results are shown in Table 3. Substantial changes in the skill rankings resulted; for example, m8 and m9 are much higher here than in Table 1, while m15 and m17 are much lower. In light of this sensitivity, we only use this ranking as a preliminary indicator for guidance in the subsequent analysis; it is not intended as an authoritative ranking of forecast quality, and thus it is not suited for designating these members as ''good'' or ''bad'' in the present case.

Taking Tables 1 and 3 in tandem, it is unclear if there are any additional patterns relating model settings to skill. Turning to qualitative analysis, in comparing the simulated reflectivity fields, the most consistent difference appears to be the development of strong isolated convection ahead of the boundary prior to the development of the back-building MCS for the higher-ranked members. (It should be noted that m15 also produces convection; see circled regions in columns 1 and 2 of Fig. 17.) Similar to the observed behavior in Fig. 5b, the warm-region cells in the higher-ranked members initiate along a weaker boundary produced by earlier convection (Fig. 18). The lower-ranked members produce this boundary as well, but plots of horizontal divergence in the boundary layer (not shown) indicate that incipient cells decay rapidly after moving off the boundary for those members. There is no clear difference between higher- and lower-ranked members in the placement or strength of the low-level convergence at this time. The crucial distinction appears to be related to buoyancy rather than dynamic forcing; Table 4 lists MUCAPE and MUCINH derived from soundings extracted from the region circled in Fig. 18b, and the higher-ranked members generally depict higher MUCAPE and no MUCINH in the immediate area. Taking the behavior of m15 into account, cell growth appears to be most consistently tied to lower MUCINH; however, the difference is very small and it seems likely that other small variations (not readily distinguishable in the hourly model output) must have contributed.

The importance of this isolated convection to the evolution of the outflow boundary in central Oklahoma is illustrated in Fig. 19, which overlays the approximate boundary positions for example higher-ranked and lower-ranked members. In the first pairing (m8 and m16), where only the higher-ranked member produces substantial convection in the warm region early on, the overlaid contours take on a ''braided'' appearance after that convection merges with the outflow boundary, indicating an along-line variation in outflow boundary speed near the merge point. Specifically, the western half of the boundary in the higher-ranked member slows down, relative to that of the lower-ranked member, while the eastern half speeds up. Similar patterns are shown by all convection/no-convection pairings examined during this study. In the second pairing, in which both members (m9 and m15) produce deep, isolated warm-region convection, the boundary in the lower-ranked member advances more rapidly than that of the higher-ranked member all along the line.

Thus, the model representation of warm-region convection seems linked to the model representation of the

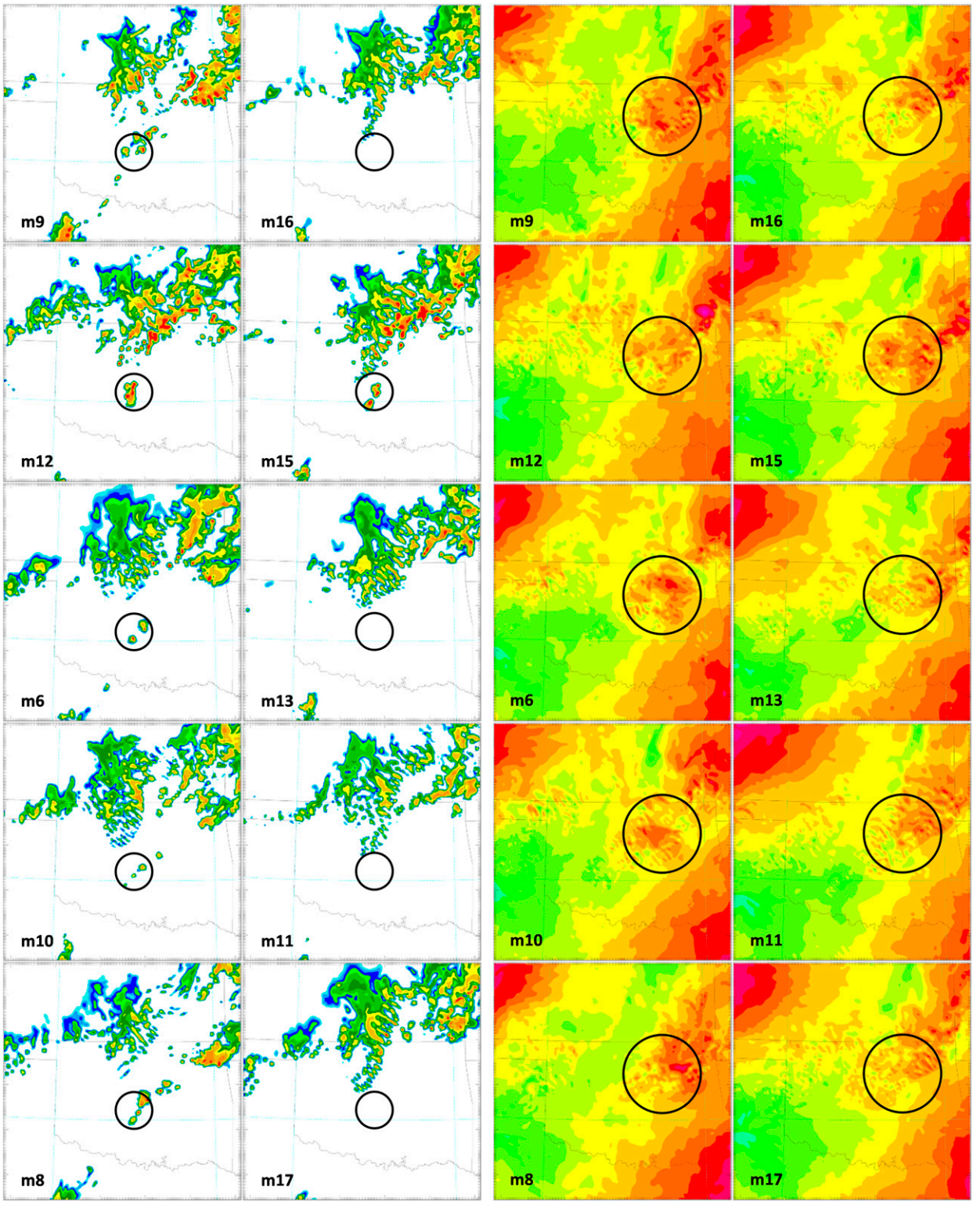

FIG. 17. The first and second columns show forecast reflectivity at 0700 UTC and the third and fourth columns show the perturbation surface pressure at 1000 UTC with stronger negative perturbations in blue, stronger positive perturbations in red, and color shifts at 1-mb intervals. Columns 1 and 3 are for higher-ranked members and columns 2 and 4 are for lower-ranked members, shown from top to bottom in order of QPF ETS as in Table 4.

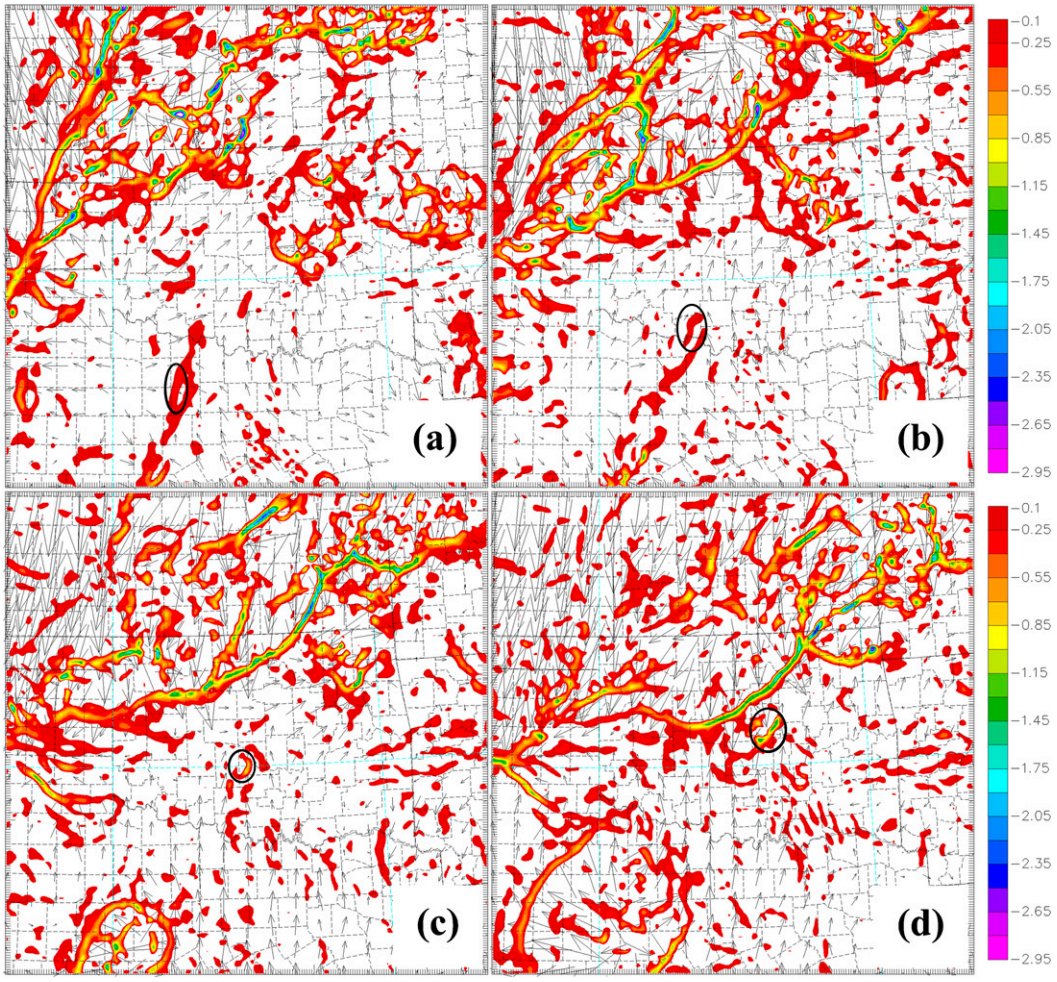

FIG. 18. Horizontal divergence (only negative values are shown) and perturbation wind vectors at roughly 250 m AGL valid (a) 0200, (b) 0400, (c) 0600, and (d) 0800 UTC for member m6. A region of convergence associated with warm-region convection is highlighted by the black circles.

reorientation of the boundary associated with the rainfall event in Oklahoma City. Plots of the surface pressure fields for all 10 members at 0600 UTC (not shown) depict a mesohigh developing in northwestern Oklahoma, behind the convective line associated with the earlier MCS. This feature moves into central Oklahoma by 1000 UTC, where it is reinforced by the warm-region convection moving in from the southwest in the higher-ranked members and m15 (see circled regions in columns 3 and 4 in Fig. 17). At the same time, falling surface pressure, rising surface temperature, and lack of precipitation (e.g., see circled regions in Fig. 20) suggest a region of dry subsidence developing over the western part of the boundary in the higher-ranked members; based on subsequent observations, we speculate that this clearing reduces frontogenesis (i.e., by hindering subsequent rainfall and evaporative cooling behind the boundary) and thus helps to slow this portion of the boundary considerably. In any event, the speed of the outflow boundary increases near the mesohigh and slows to the west; this speed differential is generally more pronounced in the higher-ranking members and thus reorients the outflow boundary at a larger angle to the low-level jet, locally enhancing lift. A new, quasi-stationary convective cluster rooted to the outflow boundary then develops between the mesohigh and the subsidence region.

Precipitation from this cluster continues to reinforce the mesohigh through evaporative cooling, and the configuration remains in place as long as the dry region persists over the western portion of the boundary. An effect of this dry region is illustrated in Figs. 20 and 21; in m8 and m9, for which the western portion of the outflow boundary remains free of precipitation through 1000 UTC, favorable outflow boundary reorientation persists during the most

TABLE 4. MUCAPE and MUCINH at the location circled in Fig. 18b valid at 0500 UTC Jun 14, as derived from forecast soundings. (The members are listed in order of descending ETS rank using the scores from Table 3.)

Member	MUCAPE (J kg^{-1})	MUCINH (J kg^{-1})
m9	2289	0
m12	2269	0
m6	2092	0
m10	2416	0
m8	2337	0
m16	2044	6
m15	2224	2
m13	2011	9
m11	2171	15
m17	1773	24

intense part of the event. On the other hand, m12 and m15 develop spurious rainfall over western Oklahoma by 1000 UTC; an attendant cooling and pressure rise subsequently drives the western portion of the boundary farther to the south, producing a less favorable orientation and causing much of the later precipitation to fall to the south and/or east of the correct location. The local decrease in forecast quality later in the period for the latter two members is suggested by the observed and predicted rainfall accumulations plotted in Fig. 6 for Oklahoma City, as well as the regional plots in Fig. 22. The midlevel conditions at 1200 UTC (Fig. 23) and plots of forecast MUCAPE in western Oklahoma (Fig. 24) suggest that the dry region was associated with subsidence near the 700-hPa jet, while the spurious precipitation in m12 and m15 arose from a surplus of buoyancy immediately ahead of the boundary.

It should be noted that m12 and m15 represent special cases and several caveats must be included in evaluating their performance. Despite a southward bias in outflow boundary position and relatively moderate forecast accumulations (Fig. 22c), m12 ranks highly in both Tables 1 and 3. This appears to be due in part to spurious cells ''fortuitously'' tracking over the area of interest in the m12 forecast. Meanwhile, despite the fact that it forecasts the outflow boundary position with similar accuracy while also forecasting the extreme accumulations (albeit with position errors) that m12 missed, m15's rank is much lower in Table 3 than in Table 1. This is a further indication of the sensitivity of the skill rankings to the details of the ETS calculations, particularly the allowance radius; the position errors of the accumulation extrema in Fig. 22d are small but greater than the 25-km allowance radius used in this study. Thus, m15's skill score suffers from double penalties in the same manner that can occur in point-to-point QPF verification, and it would clearly rank higher if a larger allowance radius was used [e.g., 50 km, as in Schumacher et al. (2013)].

To examine why m15 predicts extreme accumulation while m12 does not, plots of surface temperature and 850–500-mb (1 mb = 1 hPa) shear at 1300 UTC for the two members are shown in Fig. 25 along with the difference fields of precipitable water and accumulated precipitation for the period from 1200 to 1500 UTC. A stronger temperature gradient with vertical shear

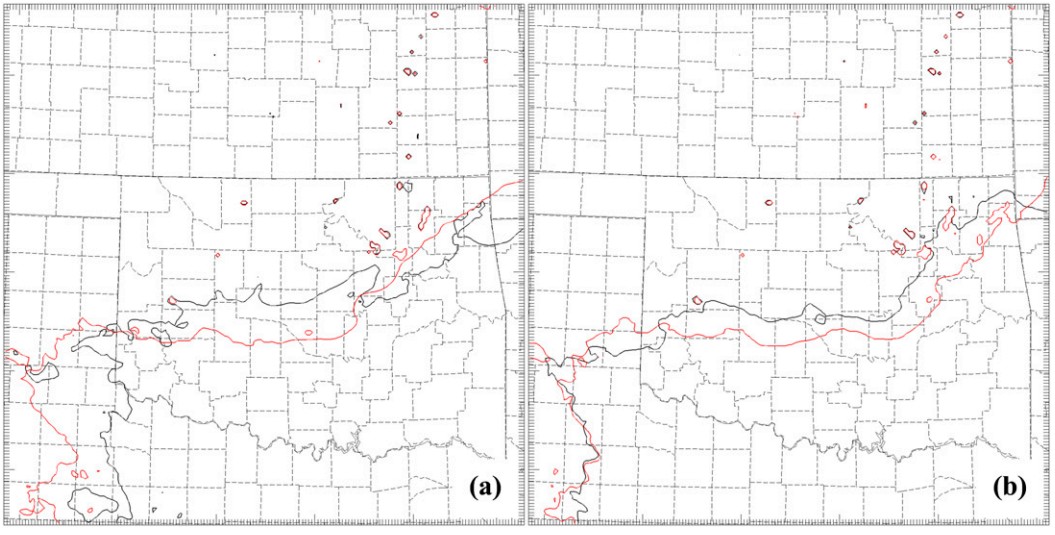

FIG. 19. (a) The 1100 UTC 72°F surface isotherms for higher-ranked m8 (black) and lower-ranked m16 (red) members. (b) As in (a), but for higher-ranked m9 (black) and lower-ranked m15 (red) members.

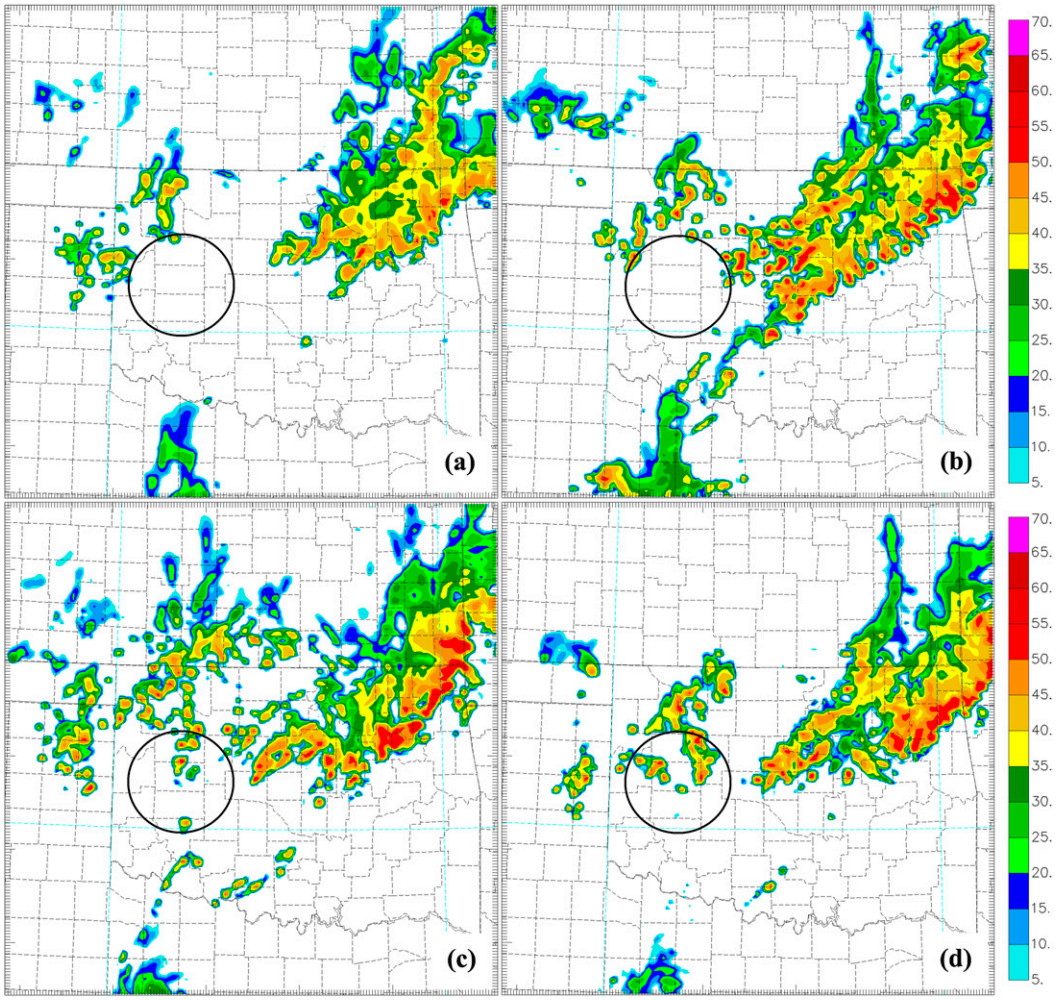

FIG. 20. Reflectivity valid at 1000 UTC for (a) m8, (b) m9, (c) m12, and (d) m15. Circles highlight clearing near the western part of the outflow boundary in higher-ranked members.

oriented somewhat more along the boundary (black circles) and a persistent region of greater moisture content (magenta circles) suggest a more favorable upstream environment in m15. However, the implications are mixed. On the one hand, while enhanced precipitable water was likely a significant factor in this event, the differences shown here are highly localized (as with the parameters related to the earlier preboundary convection) and cannot be readily linked to prior or larger-scale conditions based on the data currently available. This limits both their predictability (particularly by deterministic means) and their usefulness in this study.

On the other hand, the difference in the temperature gradient appears to stem from a difference in the strength of the cold pool (and hence the mesohigh) in northeastern Oklahoma. This is confirmed by examining Fig. 17, which shows a discernibly weaker mesohigh for m12 than for m15. Moreover, it is noted (although not shown here) in all of the members discussed in this section that convection farther from the mesohigh, or convection in members that depict a weaker pressure gradient on the western and southern sides of the mesohigh, tends to be more scattered and less coherent than what was actually observed, with Fig. 22 providing an illustrative example. This adds support to the premise that the earlier preboundary convection played a critical role, not only in triggering the back-building MCS, but also in creating an environment that enhanced its intensity by strengthening the mesohigh.

Based on this analysis, a conceptual model for this event is proposed, as illustrated in Fig. 26, with corresponding mesonet and radar observations shown in Fig. 27. By 0800 UTC, the earlier MCS had produced a mesohigh in north-central Oklahoma as isolated cells

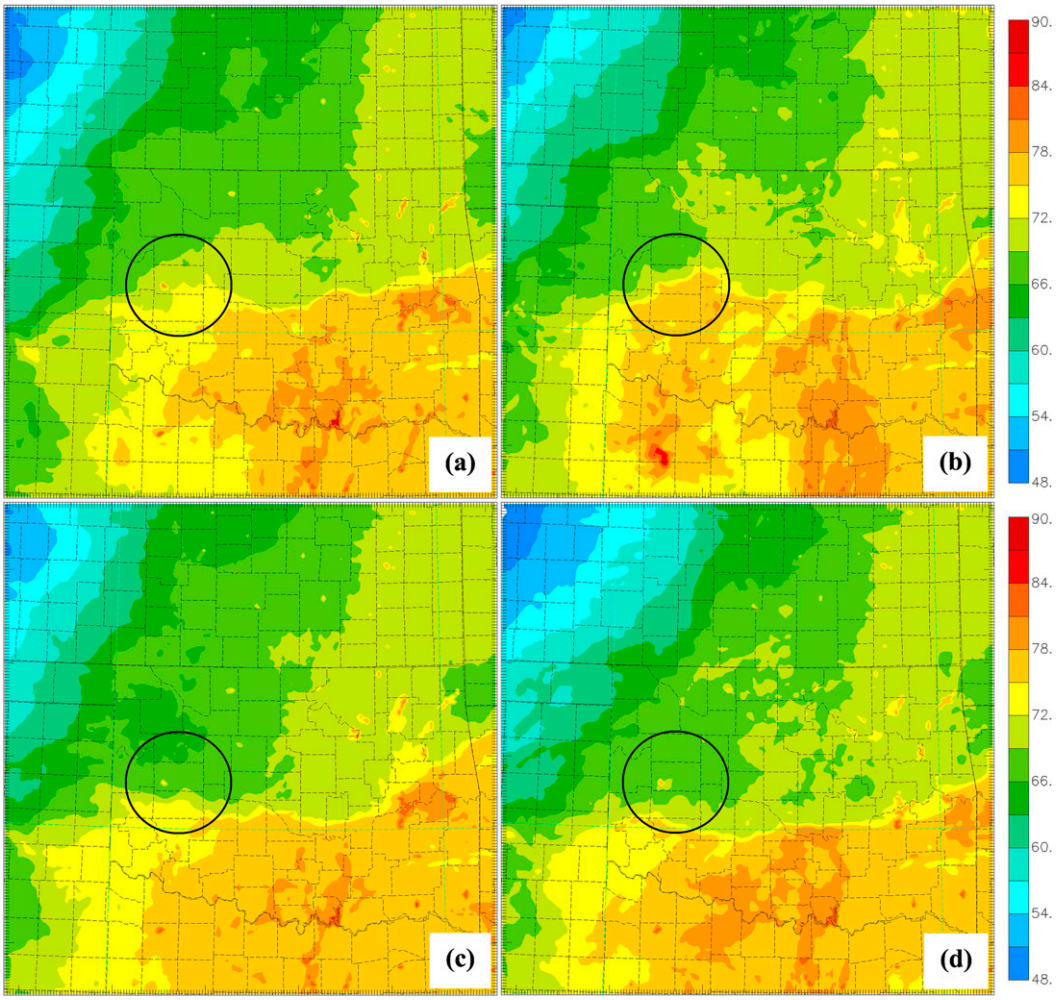

FIG. 21. As in Fig. 20, but for surface temperature valid at 1200 UTC.

developed in the warm region southwest of Oklahoma City. (Figs. 26a and 27a) By 1000 UTC, those cells had coalesced into a new MCS over the reoriented boundary, with convective precipitation moving well away from the boundary and into the mesohigh. Meanwhile, a region of subsidence developed in the wake of the earlier storms, backing the winds behind the western part of the boundary and smothering additional cells moving in from the west. (Figs. 26b and 27b)

The surface pressure analysis for this period suggests the development of a col near the subsidence region, between the mesohigh to the east and larger-scale high pressure to the west. Shortly before 1200 UTC, the MCS entered an intense back-building phase that produced over 50 mm of rain in western Oklahoma City over the next hour, with an elongated plume of intense precipitation remaining nearly stationary near the col (Figs. 26c and 27c). However, the subsidence region began to decay soon afterward as the 700-hPa jet maximum moved off to the northeast and cloud-layer winds behind the outflow boundary veered dramatically. After 1300 UTC, increasing rainfall on the western flank of the MCS gradually intensified the cold pool in central Oklahoma (Figs. 26d and 27d) until the stalled portion of the outflow boundary was forced to the south and the event ended. Thus, the mesohigh, the subsidence region, and a tenuous balance of buoyancy and convective inhibition in the warm region were all important factors in maintaining local rainfall intensity and duration in this case.

5. Summary and conclusions

An intense, localized back-building MCS produced extreme rainfall and flooding in the Oklahoma City

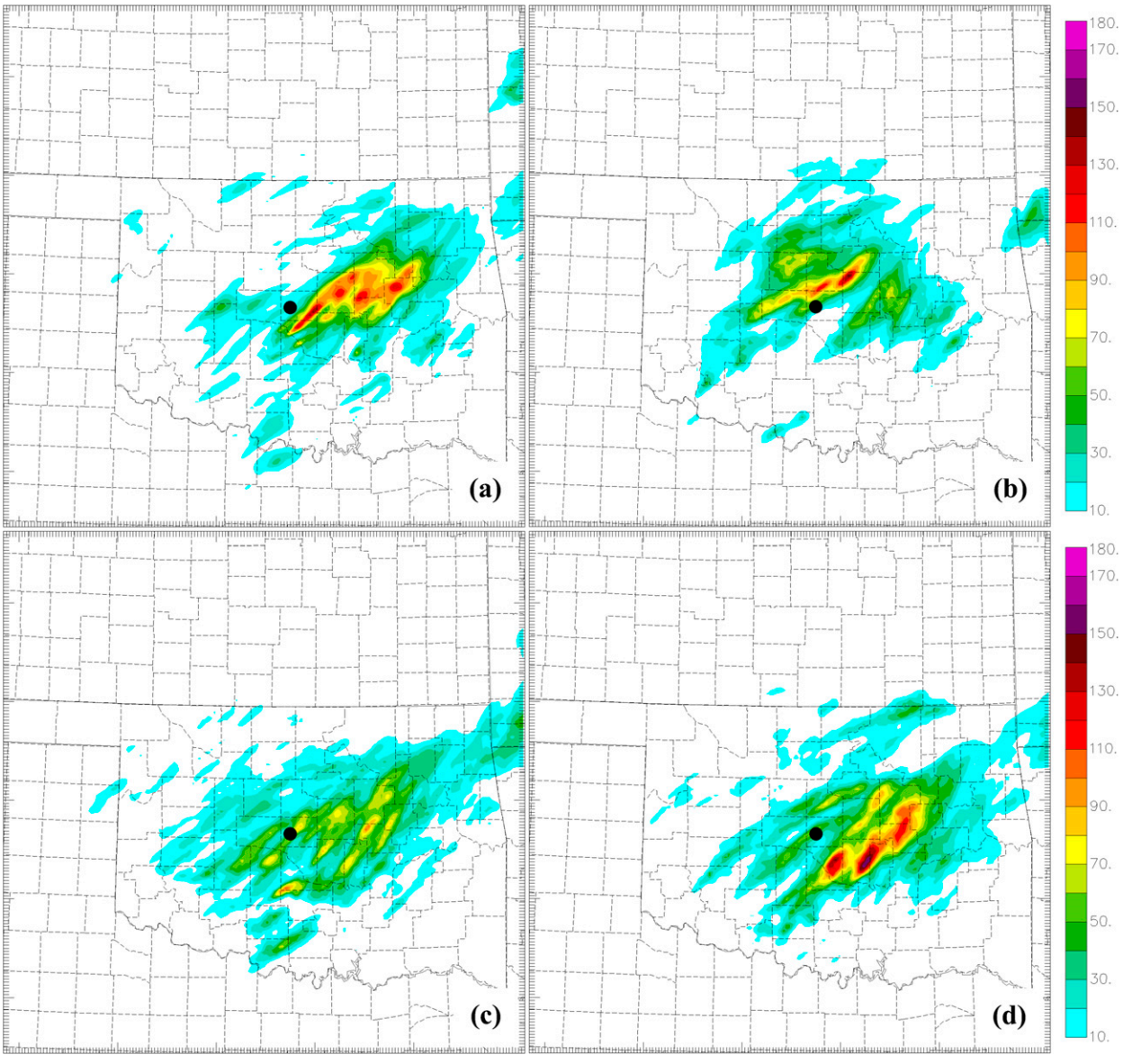

FIG. 22. The 6-h accumulated precipitation (mm) valid at 1800 UTC for (a) m8, (b) m9, (c) m12, and (d) m15. Compare with QPE plot in Fig. 7 and observed reflectivity in Fig. 25c. The black dot marks the location of Oklahoma City.

area on 14 June 2010. Because of the skill it demonstrated in this instance, CAPS Storm-Scale Ensemble Forecast output was used to examine how this event evolved. While the ensemble QPF products show a high degree of accuracy, the forecast skills of individual members differ significantly. A neighborhood-based equitable threat score evaluated from the stage IV precipitation analysis was used to rank the members in order to highlight relationships between member settings and the depiction of crucial features. In the process, errors tied specifically to the initialization procedure and physics parameterizations were brought to light. First, not assimilating radar data severely reduces forecast quality from the outset. Second, members that included additional convective-scale perturbations in the initial conditions for this high-MUCAPE/low-MUCINH environment produce widespread spurious convection (as a result of the perturbation magnitudes being too large) that persists well into the forecast, similarly diminishing forecast quality. Finally, the members using the Thompson microphysics scheme produce initial cold pools that are too weak and spread too slowly, which has a large impact on the forecast skill

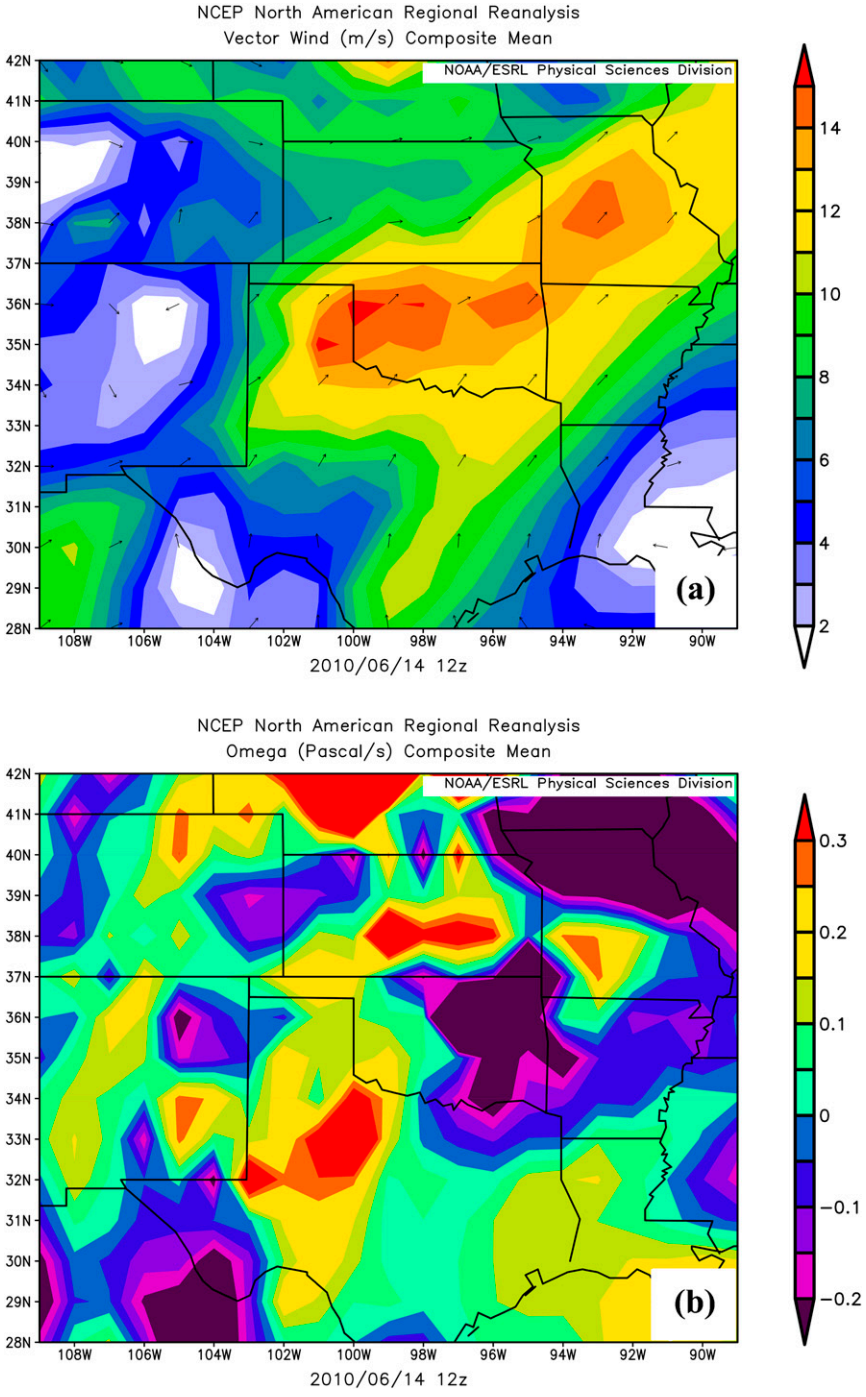

FIG. 23. The 1200 UTC North American Regional Reanalysis (a) wind ($m\,s^{-1}$) and (b) omega ($Pa\,s^{-1}$) at 700 mb. [Images taken from the ESRL archive online (http://www.esrl.noaa.gov/psd/cgi-bin/data/narr/plothour.pl).]

because of the critical role that outflow boundary forcing played in this case.

This finding of a slow cold pool bias in the Thompson members stands in contrast to the report in Clark et al. (2012) that, based on subjective evaluations, other schemes exhibited a fast cold pool bias while the Thompson scheme seemed to produce "more realistic" predictions of cold pool strength during the 2010 Spring Experiment. However, a more recent object-based statistical analysis in Clark et al. (2014) indicates a

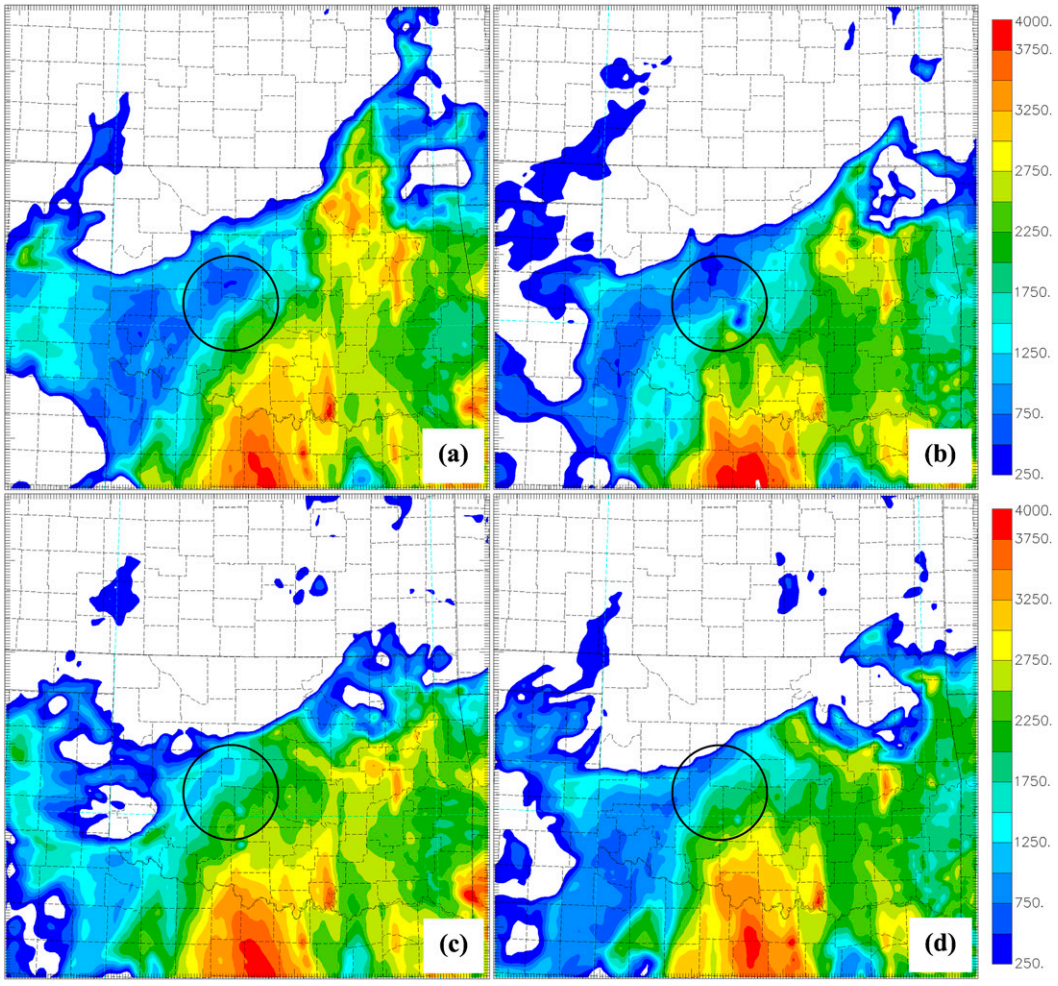

FIG. 24. As in Fig. 20, but for surface-based MUCAPE valid at 0700 UTC with circles highlighting greater buoyancy in lower-ranked members.

generally strong slow bias in MCS motion (again, attributable to generally weaker cold pools) for the Thompson members relative to observations as well as predictions from members using other microphysics schemes, which agrees with the results shown here. It must be noted that this association between the Thompson scheme and a weak, slow cold pool bias is not universal; for example, in a multimicrophysics ensemble modeling study of a warm-season squall line by Wheatley et al. (2014), the strongest cold pool and the most accurate representation of precipitation structure and intensity (particularly in the trailing stratiform region) were obtained from the Thompson scheme. The cause of the disparity has not been determined, although differences in storm environment (e.g., less MUCAPE and drier middle- and upper-level upstream conditions in the Wheatley et al. case), as well as the modeling methodology (e.g., an ensemble Kalman filter approach in Wheatley et al.), may be factors. In light of this uncertainty, it would be beneficial to obtain and examine output at greater temporal resolution for a variety of cases to obtain a more conclusive diagnosis for how (and when) the Thompson scheme may produce cold pool errors for warm-season events.

After systemic errors were determined and excluded, the remaining SSEF members were examined more intensively. Bivariate correlations between QPF skill and broad-scale aspects of the model forecast suggest that warm-region biases in temperature, moisture, and strength of the low-level jet are not significant factors for a successful forecast in this case. The area-averaged MUCAPE and MUCINH may have more value as discriminators, although a clear pattern is not demonstrated here. However, qualitative comparison between higher- and lower-ranked members revealed that small, localized variations in buoyancy may have played a role

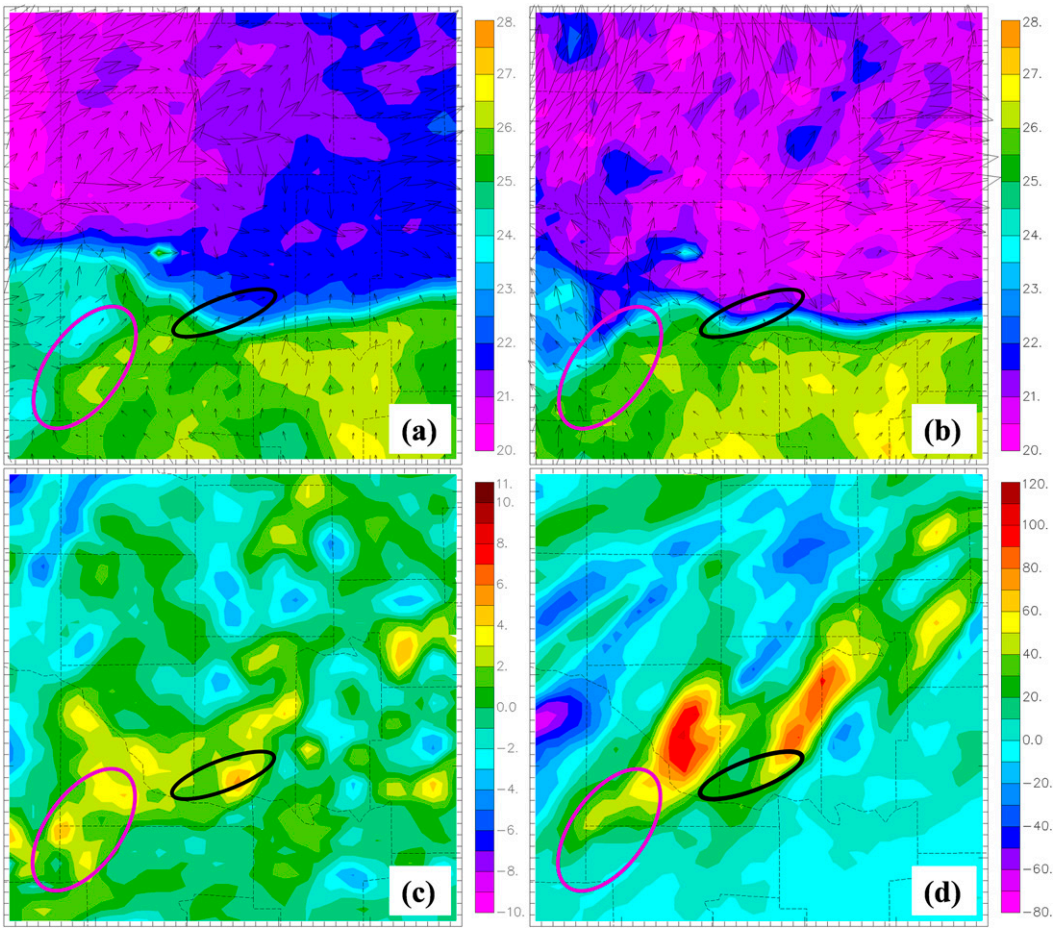

FIG. 25. (a) Observed surface temperature (°C) and 850–500-mb shear (arrows) valid at 1300 UTC for member m12. (b) As in (a), but for member m15. (c) Difference in vertically integrated precipitable water (mm) between m15 and m12, averaged from hourly output from 1200 to 1500 UTC. (d) Difference in accumulated precipitation (mm) from 1200 to 1500 UTC between m15 and m12. Black ovals highlight a stronger temperature gradient and more favorable vertical shear in m15, while magenta ovals highlight an upstream region of enhanced precipitable water in m15.

in maintaining a favorable position and orientation for the outflow boundary. For instance, a small increase in MUCINH in a specific area ahead of the boundary appears to suppress the convection responsible for triggering the back-building MCS and reinforcing the mesohigh, while an increase in MUCAPE in another area produces excessive convection and precipitation over the outflow boundary west of Oklahoma City, which prevents the boundary from stalling and reorienting correctly.

From this examination, it appears that the extreme rainfall occurred within a stalled boundary configuration similar to that detailed in Maddox et al. (1979) but lacking midlevel shear and steering winds parallel to the boundary at the time and location of the most extreme precipitation. An intense low-level jet overrunning the outflow boundary combined with the lack of shear to produce a small but vigorous back-building MCS that persisted for several hours. Furthermore, clearing to the west (possibly arising from synoptically forced subsidence) initially helped orient the outflow boundary nearly perpendicular to the low-level jet and subsequently suppressed convection that could have led to cold pool redevelopment and driven the outflow boundary (and hence the MCS) out of central Oklahoma more quickly. An apparent surface pressure col in the vicinity of the clear region may have helped strengthen the MCS during the most intense stage, although this enhancement is not established by the available data.

Clearly, the explanation for this event remains incomplete. This ensemble forecast could profitably be

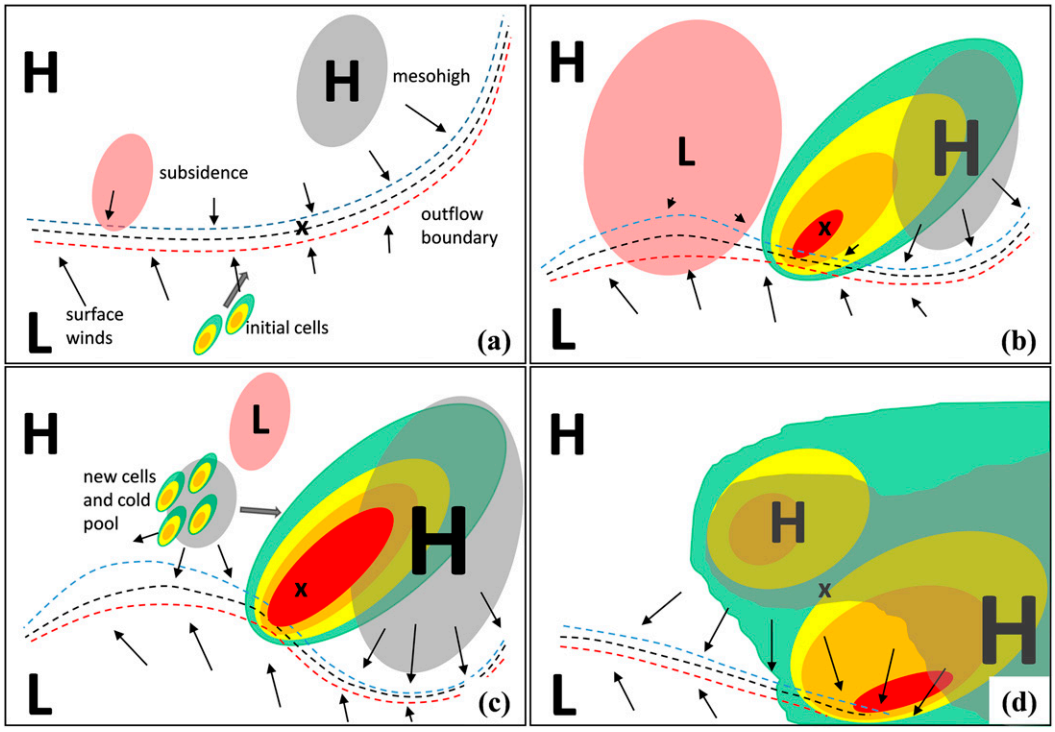

FIG. 26. Proposed event schematic showing the initiation, organization, maturation, and decay stages for the Oklahoma City MCS. (a) Isolated cells initiate in the warm region upstream from the mesohigh from an earlier MCS, while the outflow boundary stalls to the west under a region of subsidence. (b) The cells coalesce into a new MCS over the boundary, with convective precipitation falling into the mesohigh region; cooling from this precipitation contributes to faster outflow boundary motion to the east while the boundary remains stalled to the west, which reorients the boundary at a larger angle to the low-level jet. (c) The new MCS back builds and intensifies in the col between the mesohigh and larger-scale high pressure to the west, remaining in phase with the boundary; however, the midlevel winds also veer, the subsidence region erodes and moves away, and new cells and an associated cold pool form near the stalled portion of the boundary. (d) The cold pool from the new cells drives the boundary southward, ending the extreme rainfall in Oklahoma City. Midlevel winds near incipient cells are shown by gray arrows in (a) and (c), and the location of Oklahoma City is indicated by the black ×.

subjected to further examination [e.g., applying ensemble sensitivity analysis as in Bednarczyk and Ancell (2015) or Torn and Romine (2015)] to check for additional dependencies, possibly related to features even more subtle than those described here. In any case, it is clear that the 2010 Oklahoma City flood was strongly influenced by transient, small-scale variations that are unlikely to be reliably captured by a single deterministic forecast. Therefore, this case provides further evidence that the ensemble-based approach is of great value to quantitative precipitation forecasting of convective events that involve complex mesoscale and storm-scale interactions.

Acknowledgments. This study was accomplished as part of a CAPS research assistantship from NSF Grant CNS-0941491. MX was also supported by NSF Grants AGS-1046171 and AGS-1261776. The CAPS SSEF forecasts were produced under the support of NOAA NWS CSTAR program, on an NSF Xsede supercomputer at the National Institute of Computational Science (NICS) of the University of Tennessee. CAPS scientists Fanyou Kong, Kevin Thomas, Yunheng Wang, Keith Brewster, and Jidong Gao contributed to the development and running of the SSEF system. Radar and in situ verification data were obtained from the Oklahoma Mesonet and visualized using the WeatherScope software package. QPF verification data were obtained from the National Center for Environmental Prediction's stage IV archive and mapped using online code provided by Mike Baldwin. Valuable collaboration and graphics were provided by Russ Schumacher. Finally, the authors greatly appreciate the critiques and insights provided by the reviewers for this paper, through which its quality was substantially improved.

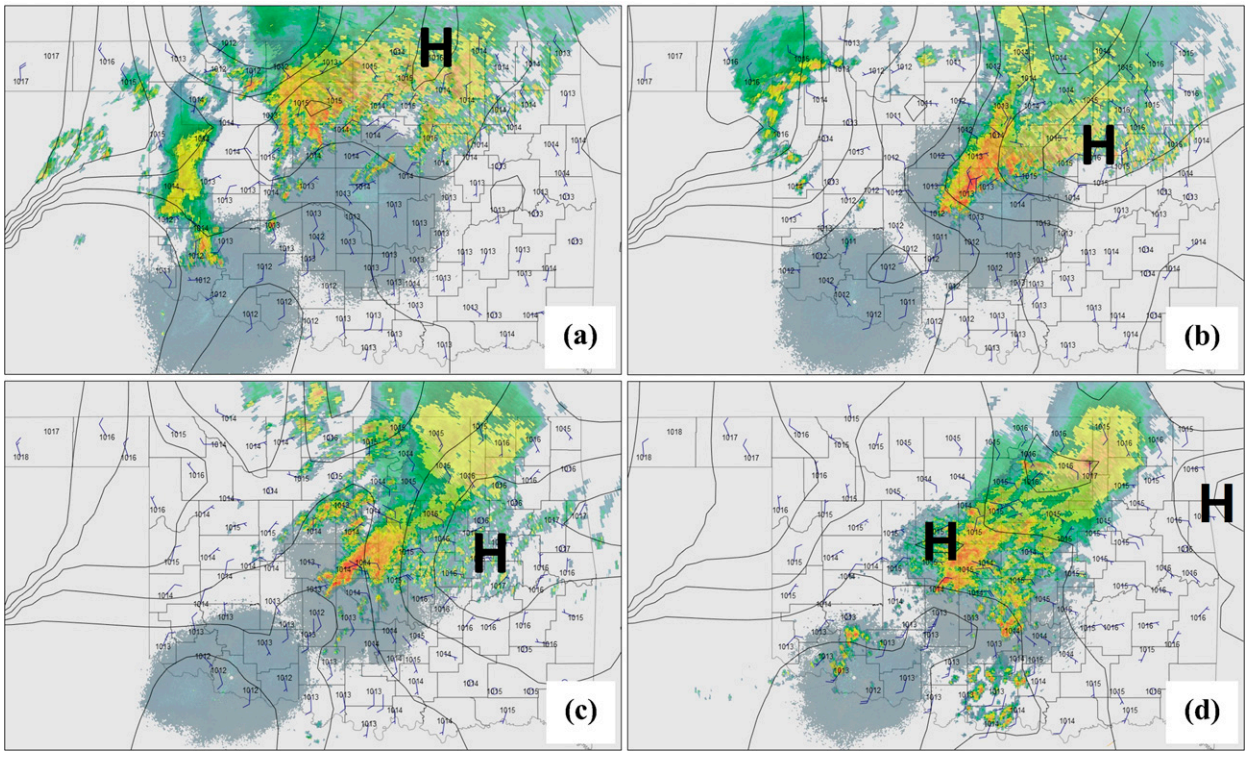

FIG. 27. Observed mean sea level pressure (black contours; hPa) and winds with the observed reflectivity mosaic overlaid valid at (a) 0800, (b) 1000, (c) 1230, and (d) 1430 UTC. The approximate locations of mesohighs are marked with an H.

REFERENCES

Basara, J. B., B. G. Illston, and G. D. McManus, 2011: Atmospheric contributors to the 14 June 2010 flash flood in Oklahoma City. *Proc. Int. Symp. on Earth-Science Challenges*, Norman, OK, University of Oklahoma–Kyoto University, Paper ID 64.

Bednarczyk, C. N., and B. C. Ancell, 2015: Ensemble sensitivity analysis applied to a southern plains convective event. *Mon. Wea. Rev.*, **143**, 230–249, doi:10.1175/MWR-D-13-00321.1.

Blackadar, A. K., 1957: Boundary layer wind maxima and their significance for the growth of nocturnal inversions. *Bull. Amer. Meteor. Soc.*, **38**, 283–290.

Bryan, G. H., and H. Morrison, 2012: Sensitivity of a simulated squall line to horizontal resolution and parameterization of microphysics. *Mon. Wea. Rev.*, **140**, 202–225, doi:10.1175/MWR-D-11-00046.1.

——, J. C. Wyngaard, and J. M. Fritsch, 2003: Resolution requirements for the simulation of deep moist convection. *Mon. Wea. Rev.*, **131**, 2394–2416, doi:10.1175/1520-0493(2003)131<2394:RRFTSO>2.0.CO;2.

Bukovsky, M. S., J. S. Kain, and M. E. Baldwin, 2006: Bowing convective systems in a popular operation model: Are they for real? *Wea. Forecasting*, **21**, 307–324, doi:10.1175/WAF908.1.

Clark, A. J., W. A. Gallus Jr., M. Xue, and F. Kong, 2009: A comparison of precipitation forecast skill between small convection-allowing and large convection-parameterizing ensembles. *Wea. Forecasting*, **24**, 1121–1140, doi:10.1175/2009WAF2222222.1.

——, ——, and M. L. Weisman, 2010a: Neighborhood-based verification of precipitation forecasts from convection-allowing NCAR WRF model simulations and the operational NAM. *Wea. Forecasting*, **25**, 1495–1509, doi:10.1175/2010WAF2222404.1.

——, ——, M. Xue, and F. Kong, 2010b: Convection-allowing and convection-parameterizing ensemble forecasts of a mesoscale convective vortex and associated severe weather. *Wea. Forecasting*, **25**, 1052–1081, doi:10.1175/2010WAF2222390.1.

——, and Coauthors, 2012: An overview of the 2010 Hazardous Weather Testbed Experimental Forecast Program Spring Experiment. *Bull. Amer. Meteor. Soc.*, **93**, 55–74, doi:10.1175/BAMS-D-11-00040.1.

——, R. G. Bullock, T. L. Jensen, M. Xue, and F. Kong, 2014: Application of object-based time-domain diagnostics for tracking precipitation systems in convection-allowing models. *Wea. Forecasting*, **29**, 517–542, doi:10.1175/WAF-D-13-00098.1.

Corfidi, S. F., J. H. Merritt, and J. M. Fritsch, 1996: Predicting the movement of mesoscale convective complexes. *Wea. Forecasting*, **11**, 41–46, doi:10.1175/1520-0434(1996)011<0041:PTMOMC>2.0.CO;2.

Davis, C. A., K. W. Manning, R. E. Carbone, S. B. Trier, and J. D. Tuttle, 2003: Coherence of warm season continental rainfall in numerical weather prediction models. *Mon. Wea. Rev.*, **131**, 2667–2679, doi:10.1175/1520-0493(2003)131<2667:COWCRI>2.0.CO;2.

Dawson, D. T., M. Xue, J. A. Milbrandt, and M. K. Yau, 2010: Comparison of evaporation and cold pool development between single-moment and multimoment bulk microphysics schemes in idealized simulations of tornadic thunderstorms. *Mon. Wea. Rev.*, **138**, 1152–1171, doi:10.1175/2009MWR2956.1.

Doswell, C. A., III, H. E. Brooks, and R. A. Maddox, 1996: Flash flood forecasting: An ingredients-based methodology. *Wea. Forecasting*, **11**, 560–581, doi:10.1175/1520-0434(1996)011<0560:FFFAIB>2.0.CO;2.

Ebert, E. E., 2001: Ability of a poor man's ensemble to predict the probability and distribution of precipitation. *Mon. Wea. Rev.*, **129**, 2461–2480, doi:10.1175/1520-0493(2001)129<2461:AOAPMS>2.0.CO;2.

Hawblitzel, D. P., F. Zhang, Z. Meng, and C. A. Davis, 2007: Probabilistic evaluation of the dynamics and predictability of the mesoscale convective vortex of 10–13 June 2003. *Mon. Wea. Rev.*, **135**, 1544–1563, doi:10.1175/MWR3346.1.

Heideman, K. F., and J. M. Fritsch, 1988: Forcing mechanisms and other characteristics of significant summertime precipitation. *Wea. Forecasting*, **3**, 115–130, doi:10.1175/1520-0434(1988)003<0115:FMAOCO>2.0.CO;2.

Hohenegger, C., and C. Schär, 2007: Atmospheric predictability at synoptic versus cloud-resolving scales. *Bull. Amer. Meteor. Soc.*, **88**, 1783–1793, doi:10.1175/BAMS-88-11-1783.

Hu, M., M. Xue, and K. Brewster, 2006: 3DVAR and cloud analysis with WSR-88D level-II data for the prediction of the Fort Worth tornadic thunderstorms. Part I: Cloud analysis and its impact. *Mon. Wea. Rev.*, **134**, 675–698, doi:10.1175/MWR3092.1.

Hu, X.-M., J. W. Nielsen-Gammon, and F. Zhang, 2010: Evaluation of three planetary boundary layer schemes in the WRF model. *J. Appl. Meteor. Climatol.*, **49**, 1831–1844, doi:10.1175/2010JAMC2432.1.

Johnson, A., and Coauthors, 2014: Multiscale characteristics and evolution of perturbations for warm season convection-allowing precipitation forecasts: Dependence on background flow and method of perturbation. *Mon. Wea. Rev.*, **142**, 1053–1073, doi:10.1175/MWR-D-13-00204.1.

Junker, N. W., R. S. Schneider, and S. L. Fauver, 1999: A study of heavy rainfall events during the great Midwest flood of 1993. *Wea. Forecasting*, **14**, 701–712, doi:10.1175/1520-0434(1999)014<0701:ASOHRE>2.0.CO;2.

Kong, F., K. K. Droegemeier, and N. L. Hickmon, 2006: Multiresolution ensemble forecasts of an observed tornadic thunderstorm system. Part I: Comparison of coarse and fine-grid experiments. *Mon. Wea. Rev.*, **134**, 807–833, doi:10.1175/MWR3097.1.

——, ——, and ——, 2007: Multiresolution ensemble forecasts of an observed tornadic thunderstorm system. Part II: Storm-scale experiments. *Mon. Wea. Rev.*, **135**, 759–782, doi:10.1175/MWR3323.1.

Lim, K.-S., and S.-Y. Hong, 2010: Development of an effective double-moment cloud microphysics scheme with prognostic cloud condensation nuclei (CCN) for weather and climate models. *Mon. Wea. Rev.*, **138**, 1587–1612, doi:10.1175/2009MWR2968.1.

Lin, Y., and K. E. Mitchell, 2005: The NCEP stage II/IV hourly precipitation analyses: Development and applications. Preprints, *19th Conf. on Hydrology*, San Diego, CA, Amer. Meteor. Soc., 1.2. [Available online at http://ams.confex.com/ams/Annual2005/techprogram/paper_83847.htm.]

Maddox, R. A., C. F. Chappell, and L. R. Hoxit, 1979: Synoptic and meso-α aspects of flash flood event. *Bull. Amer. Meteor. Soc.*, **60**, 115–123, doi:10.1175/1520-0477-60.2.115.

Martin, W. J., and M. Xue, 2006: Sensitivity analysis of convection of the 24 May 2002 IHOP case using very large ensembles. *Mon. Wea. Rev.*, **134**, 192–207, doi:10.1175/MWR3061.1.

Molinari, J., and M. Dudek, 1992: Parameterization of convective precipitation in mesoscale numerical models: A critical review. *Mon. Wea. Rev.*, **120**, 326–344, doi:10.1175/1520-0493(1992)120<0326:POCPIM>2.0.CO;2.

Moore, J. T., F. H. Glass, C. E. Graves, S. M. Rochette, and M. J. Singer, 2003: The environment of warm-season elevated thunderstorms associated with heavy rainfall over the central Unites States. *Wea. Forecasting*, **18**, 861–878, doi:10.1175/1520-0434(2003)018<0861:TEOWET>2.0.CO;2.

Parker, M. D., and R. H. Johnson, 2000: Organizational modes of midlatitude mesoscale convective systems. *Mon. Wea. Rev.*, **128**, 3413–3436, doi:10.1175/1520-0493(2001)129<3413:OMOMMC>2.0.CO;2.

Powell, S. W., R. A. Houze, A. Kumar, and S. A. McFarlane, 2012: Comparison of simulated and observed continental tropical anvil clouds and their radiative heating profiles. *J. Atmos. Sci.*, **69**, 2662–2681, doi:10.1175/JAS-D-11-0251.1.

Schumacher, R. S., 2011: Ensemble-based analysis of factors leading to the development of a multiday warm-season heavy rain event. *Mon. Wea. Rev.*, **139**, 3016–3035, doi:10.1175/MWR-D-10-05022.1.

——, and R. H. Johnson, 2005: Organization and environmental properties of extreme-rain-producing mesoscale convective systems. *Mon. Wea. Rev.*, **133**, 961–976, doi:10.1175/MWR2899.1.

——, A. J. Clark, M. Xue, and F. Kong, 2013: Factors influencing the development and maintenance of nocturnal heavy-rain-producing convective systems in a storm-scale ensemble. *Mon. Wea. Rev.*, **141**, 2778–2801, doi:10.1175/MWR-D-12-00239.1.

Stratman, D. R., M. C. Coniglio, S. E. Koch, and M. Xue, 2013: Use of multiple verification methods to evaluate forecasts of convection from hot- and cold-start convection-allowing models. *Wea. Forecasting*, **28**, 119–138, doi:10.1175/WAF-D-12-00022.1.

Thompson, G., R. M. Rasmussen, and K. Manning, 2004: Explicit forecasts of winter precipitation using an improved bulk microphysics scheme. Part I: Description and sensitivity analysis. *Mon. Wea. Rev.*, **132**, 519–542, doi:10.1175/1520-0493(2004)132<0519:EFOWPU>2.0.CO;2.

Torn, R. D., and G. S. Romine, 2015: Sensitivity of central Oklahoma convection forecasts to upstream potential vorticity anomalies during two strongly forced cases during MPEX. *Mon. Wea. Rev.*, **143**, 4064–4087, doi:10.1175/MWR-D-15-0085.1.

Wheatley, D. M., N. Yussouf, and D. J. Stensrud, 2014: Ensemble Kalman filter analyses and forecasts of a severe mesoscale convective system using different choices of microphysics schemes. *Mon. Wea. Rev.*, **142**, 3243–3263, doi:10.1175/MWR-D-13-00260.1.

Xue, M., D. Wang, J. Gao, K. Brewster, and K. K. Droegemeier, 2003: The Advanced Regional Prediction System (ARPS), storm-scale numerical weather prediction and data assimilation. *Meteor. Atmos. Phys.*, **82**, 139–170, doi:10.1007/s00703-001-0595-6.

——, and Coauthors, 2007: CAPS realtime storm-scale ensemble and high-resolution forecasts as part of the NOAA Hazardous Weather Testbed 2007 Spring Experiment. Preprints, *22nd Conf. on Weather Analysis and Forecasting/18th Conf. on Numerical Weather Prediction*, Salt Lake City, UT, Amer. Meteor. Soc., 3B.1. [Available online at https://ams.confex.com/ams/22WAF18NWP/techprogram/paper_124587.htm.]

——, and Coauthors, 2009: CAPS realtime multi-model convection-allowing ensemble and 1-km convection-resolving forecasts for

the NOAA Hazardous Weather Testbed 2009 Spring Experiment. Preprints, *23nd Conf. on Weather Analysis and Forecasting/19th Conf. on Numerical Weather Prediction*, Omaha, NE, Amer. Meteor. Soc., 16A.2. [Available online at https://ams.confex.com/ams/23WAF19NWP/techprogram/paper_154323.htm.]

——, and Coauthors, 2010: CAPS realtime storm scale ensemble and high resolution forecasts for the NOAA Hazardous Weather Testbed 2010 Spring Experiment. Preprints, *25th Conf. on Severe Local Storms*, Denver, CO, Amer. Meteor. Soc., 7B.3. [Available online at https://ams.confex.com/ams/25SLS/techprogram/paper_176056.htm.]

——, F. Kong, K. W. Thomas, J. Gao, Y. Wang, K. A. Brewster, and K. K. Droegemeier, 2013: Prediction of convective storms at convection-resolving 1 km resolution over continental United States with radar data assimilation: An example case of 26 May 2008 and precipitation forecasts from spring 2009. *Adv. Meteor.*, **2013**, 259052, doi:10.1155/2013/259052.

Zhang, F., A. M. Odins, and J. W. Nielsen-Gammon, 2006: Mesoscale predictability of an extreme warm-season precipitation event. *Wea. Forecasting*, **21**, 149–166, doi:10.1175/WAF909.1.